



Microstructure and mechanical properties of cold spray additive manufactured and post heat treated high-entropy alloys with mixed CoCrFeNi and Ti powders

Xiaping Fan^a, Xin Chu^{b, **}, Yingchun Xie^b, Dawei Zhou^a, Qingxu Tian^a, Yang Tong^a, Peter K. Liaw^c, Shuying Chen^{a, ***}, Fanchao Meng^{a,*}

^a Institute for Advanced Studies in Precision Materials, Yantai University, Yantai, Shandong, 264005, China

^b Institute of New Materials, Guangdong Academy of Sciences, National Engineering Laboratory for Modern Materials Surface Engineering Technology, Guangzhou, Guangdong, 510650, China

^c Department of Materials Science and Engineering, The University of Tennessee, Knoxville, TN, 37996, USA



ARTICLE INFO

Keywords:

Cold spray
High-entropy alloy
CoCrFeNi
Microstructure
Mechanical properties

ABSTRACT

Solid-state cold spray additive manufacturing has the potential to fabricate high-strength bulk high-entropy alloys (HEAs). Through systematic experiments, this study examined the microstructure and mechanical properties of cold spray fabricated bulk HEAs with mixed CoCrFeNi and Ti powders and explored the effects of Ti content in 4 and 7 at% and post-heat treatment at 800 °C/6 h and 1000 °C/6 h. It is found that the bulk HEAs are highly densified and remain nearly defect-free after the post-heat treatment. The addition of Ti serves as an mixing powder effect to further densify the alloys. Moreover, the addition of Ti and post-heat treatment promote the formation of fine precipitates, including Fe₂Ti, Co₂Ti, CrFe, CoTi₂, and Ni₃Ti, which contributes to the strengthening of the alloys. Furthermore, post-heat treatment improves the cohesion of the alloys and yields fine and relatively uniform grains by stimulating static recovery and recrystallization. These synergistic effects improve the hardness, elastic modulus, strength, and ductility properties. The average hardness and elastic modulus of the bulk alloys are as high as 377.6 HV and 94.8 GPa, respectively; the best ultimate tensile strength and elongation to failure are 626.7 MPa and 22.1 %, respectively. Synchrotron X-ray diffraction validates the complex precipitates formed and confirms that there is no phase change during tension. The study offers insights into the microstructure and mechanical properties of cold spray additive manufactured HEAs and the effects of mixed powders and post-heat treatment on tuning microstructure and properties.

1. Introduction

High-entropy alloys (HEAs) are comprised of five or more principal elements with compositions in 5–35 atomic percentage [1–3]. Thanks to their high configurational entropy, HEAs possess fascinating mechanical and physical properties, including high strength and ductility [4,5] as well as remarkable oxidation [6], creep [7], and fatigue resistance [8], which have promised huge potentials for industrial applications [9–14]. Moreover, the high mixing entropy is beneficial for HEAs to form stable single solid-solution structures [15,16]. However, the single-phase structured HEAs suffer from the trade-off between strength and

ductility [17,18], for example, FCC HEAs often possess high ductility but low strength [19–22], which is detrimental to structural applications. In this regard, introducing additive elements (Al, Ti, Ni, Cu, etc.) to tune the properties of HEAs has been widely reported. For instance, Oh et al. [23] explored the phase separation and mechanical behavior of AlCoCrFeNi-X (X = Cu, Mn, and Ti) HEAs and elucidated the complex phases formed and the origin of the superior strength from nanoscale BCC/B2 matrix and high modulus and hard σ-phases. Shun et al. [24] found that with the addition of Ti, R, and (Cr, Fe)-rich σ phases were formed in the CoCrFeNiTi_{0.3} HEA, which resulted in a compressive strength as high as 1529 MPa and a fracture strain of 0.60. Sun et al. [25]

* Corresponding author.

** Corresponding author.

*** Corresponding author.

E-mail addresses: chuxin@gdinm.com (X. Chu), sychen@ytu.edu.cn (S. Chen), mengfanchao@ytu.edu.cn (F. Meng).

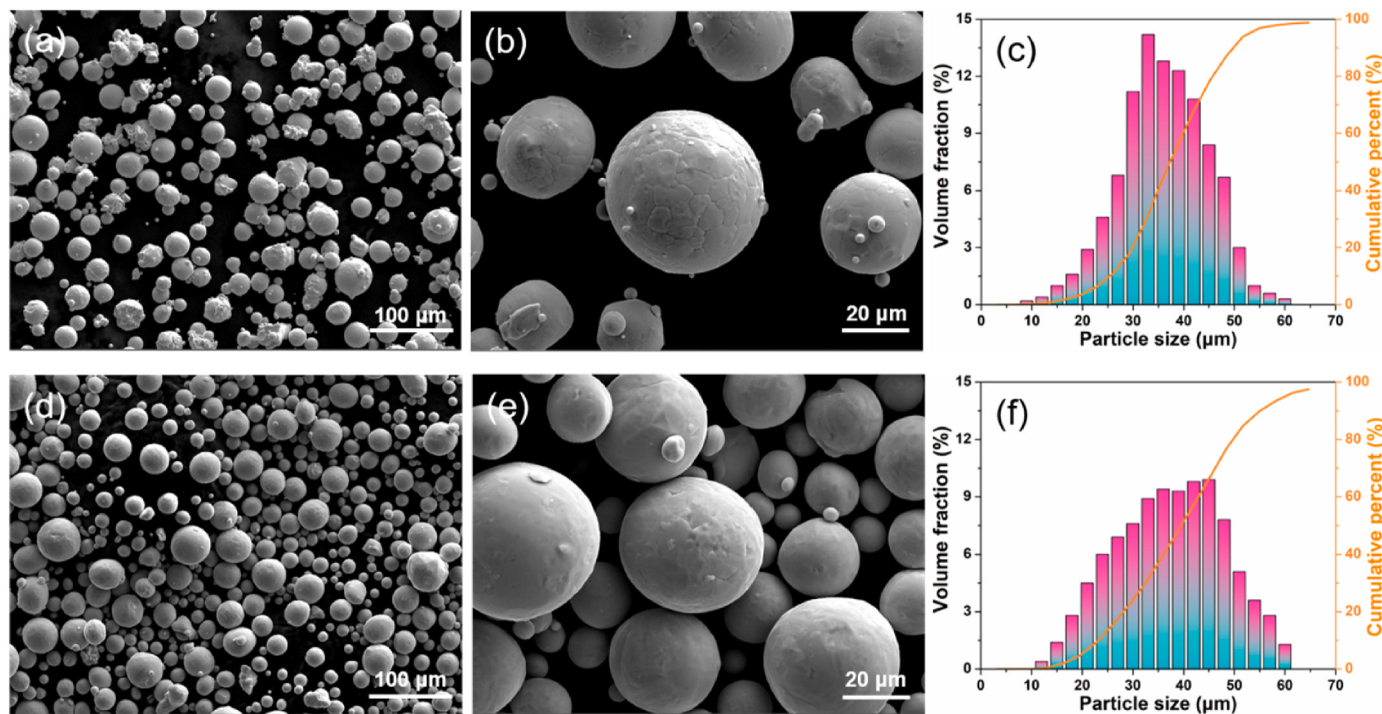


Fig. 1. Morphologies under different scanning electron microscopy magnifications and size distributions of the (a–c) CoCrFeNi powders and (d–f) Ti powders.

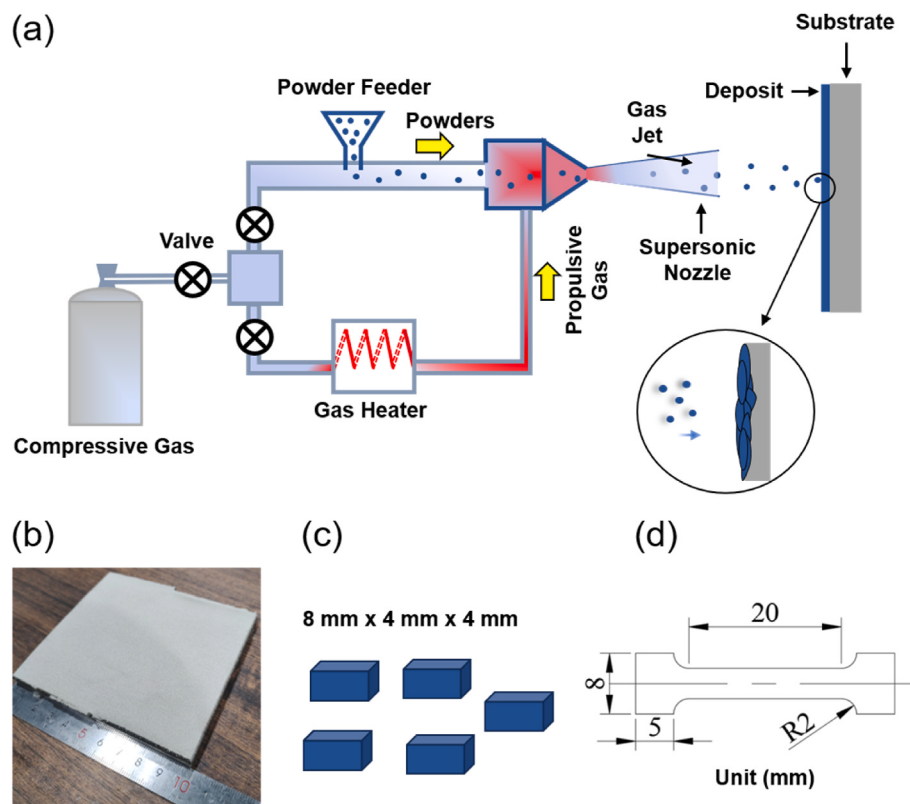


Fig. 2. (a) Schematic diagram of the cold spray process. (b) Cold spray fabricated bulk HEA. (c) and (d) depict the dimensions of the samples for characterizations and tensile tests, respectively.

investigated CoCrFeNi($\text{Al}_{0.3}\text{Ti}_{0.2}$)_x HEA and demonstrated that the γ' Ni₃(Al, Ti) phase significantly improved its mechanical properties. Karimzadeh et al. [26] also reported that the precipitation of the R-phase in CoCrFeNi HEAs by adding the Ti element helped improve the

mechanical properties.

Besides the approach of additive elements, advanced manufacturing technologies have also been widely employed to tune the microstructure and mechanical properties of HEAs [27], such as additive manufacturing

Table 1

Post-heat treatment processing parameters for the cold sprayed bulk HEAs. The parenthesis in the first column is an alternative denotation for the HEAs.

Bulk HEAs	Post-heat treatment conditions	
CoCrFeNi (Ti_0)	800 °C/6 h	1000 °C/6 h
CoCrFeNi + 4 at% Ti (Ti_4)	800 °C/6 h	1000 °C/6 h
CoCrFeNi + 7 at% Ti (Ti_7)	800 °C/6 h	1000 °C/6 h

[27–29] and powder metallurgy [9,23]. Among these methods, solid-state cold spray additive manufacturing is an appealing method because it operates powders well below their melting temperatures to impact a substrate at supersonic speeds [30,31]. Therefore, adverse effects resulting from melting-solidification processes, such as phase transformation, oxidation, and residual thermal stress accumulation, can be effectively alleviated. Recently, Ahn et al. [32] cold sprayed dense CoCrFeNiMn HEA coating of about 1 mm thick and found that the resultant hardness was more than three times larger than the cast alloy owing to process-induced ultrafine grains, high dislocation density, and nano twinning. Rojas et al. [33] cold spray additive manufactured 9 mm thick bulk CoCrFe_{0.75}NiMo_{0.3}Nb_{0.125} HEA with an excellent compressive yield strength of ~1.745 GPa and compressive ultimate strength of ~2.622 GPa, which was mainly attributed to grain boundary strengthening and work hardening by cold spray. Therefore, cold spray offers an effective route to improve strength and hardness of HEAs.

Albeit its ultra-high strain rate deposition, powder particle boundaries and micropores might exist in the cold spray deposits, which result in poor ductility of the HEAs prepared by cold spray [32–34]. Many research efforts have been paid to improve the cohesion and thereby the

ductility of the cold spray deposits, including powder design [35], mix of hard and soft powders [36], powder pre-heat treatment [37], in-situ micro-forging-assisted [38] or laser-assisted [39] cold spray, and post-treatment (post-heat [40], laser remelting [41], friction stir [42], hot-rolling [43], and hot isostatic pressing [44] treatment). Among these approaches, mixing powders and post-heat treatment are relatively easy to implement yet yield an obvious effect by improving deposition efficiency [36,45,46] and promoting atomic diffusion and recrystallization [32,34,47], respectively. Ahn et al. [32] post heat treated cold sprayed CoCrFeNiMn HEA coatings and found that appropriate heat treatment conditions helped improve ductility while affecting minimally on hardness. Feng et al. [34] studied post-heat treatment on microstructure and mechanical properties of cold sprayed bulk CoCrFeMnNi HEA. The authors found that static recovery and recrystallization occurred at 650 °C/1 h post-heat treatment and the hardness of the HEA remained higher than that of the cast alloy.

Therefore, inspired by the advantage of HEAs and cold spray additive manufacturing and their associated property tuning approaches, the present study aims to clarify the effects of combining mixed powders and post-heat treatment on tuning the microstructure and mechanical properties of cold spray additive manufactured bulk HEAs. It is speculated that mixing powders and post-heat treatment can not only increase the cohesion of the deposit but also form precipitate strengthening, which together result in hardness/strength and ductility synergy. Soft CoCrFeNi and hard Ti powders were selected to fabricate bulk HEAs using cold spray additive manufacturing. Then, the effects of Ti contents (0, 4, and 7 at%) and post-heat treatment temperatures (800 and 1000 °C) on the microstructure and mechanical properties of (CoCrFeNi)_{1-x} + Ti_x HEAs and the underlying mechanisms were examined by

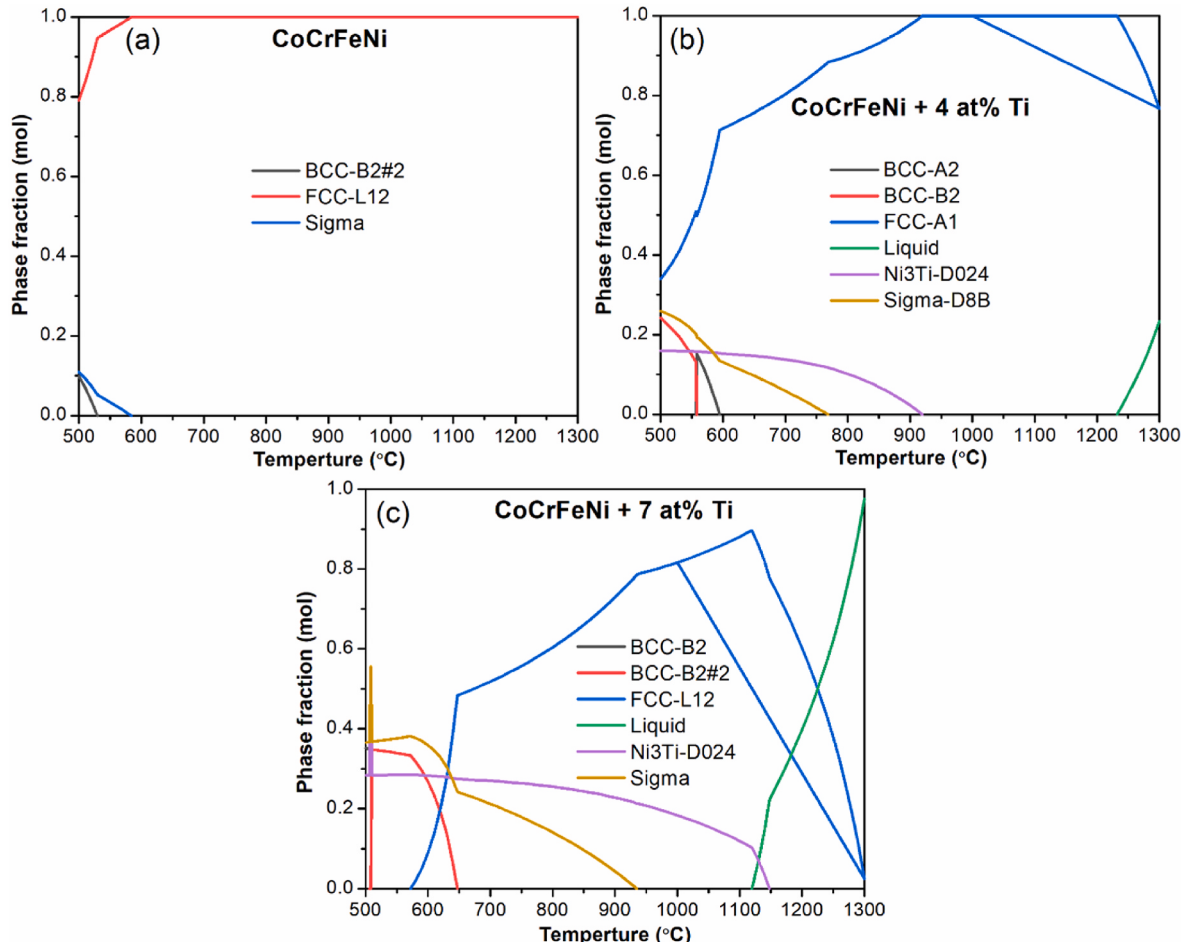


Fig. 3. Phase fractions of bulk HEAs calculated in the temperature range of 500–1300 °C of (a) CoCrFeNi, (b) CoCrFeNi + 4 at% Ti, and (c) CoCrFeNi + 7 at% Ti.

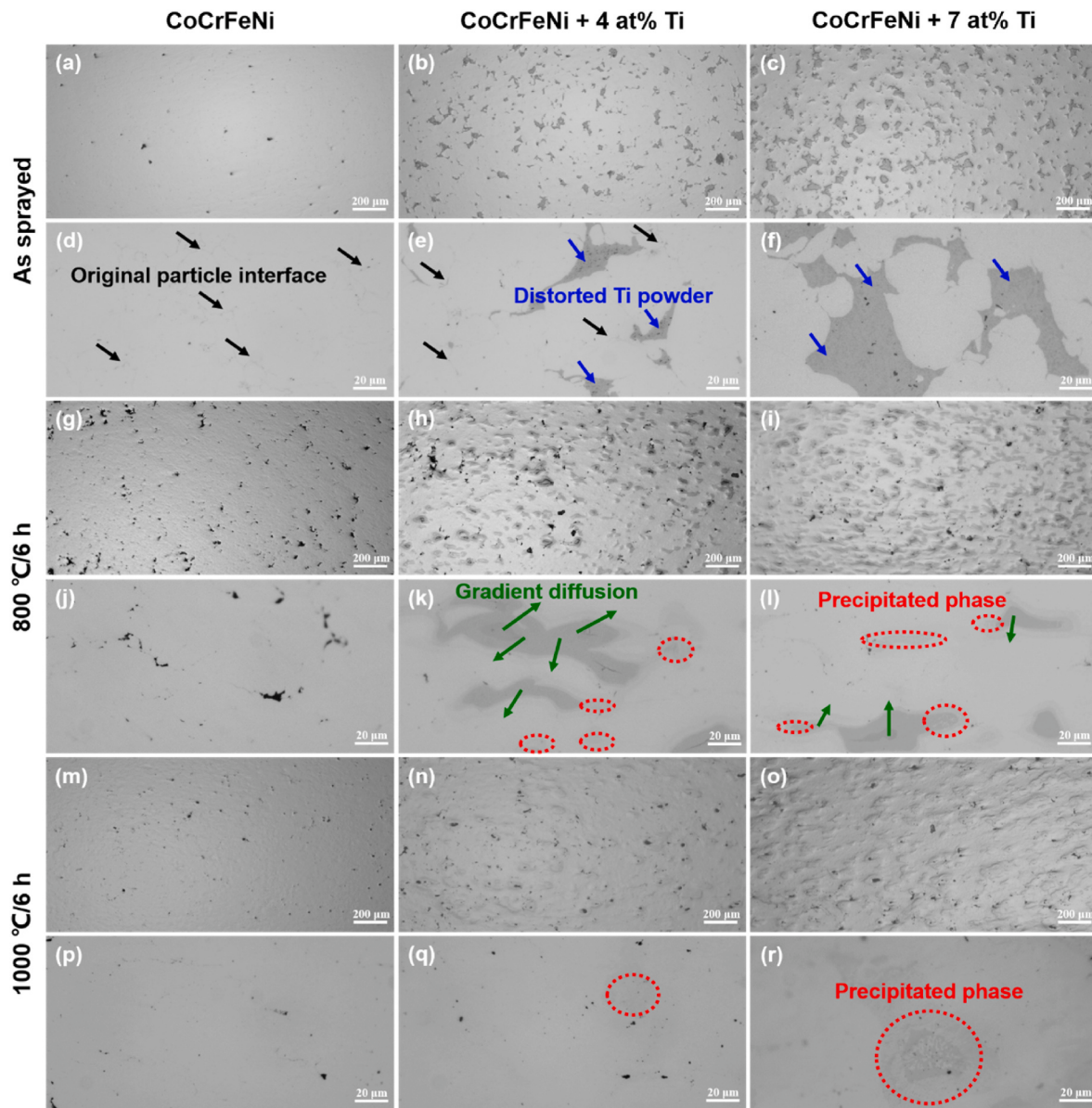


Fig. 4. Optical micrographs of bulk HEAs of CoCrFeNi (the first column), CoCrFeNi + 4 at% Ti (the second column), and CoCrFeNi + 7 at% Ti (the third column) under conditions in (a–f) as sprayed, (g–l) 800 °C/6 h, and (m–r) 1000 °C/6 h. The black, blue, and olive arrows indicate the original particle interface, distorted Ti powder, and the formed gradient diffusion zone from Ti powders to the CoCrFeNi matrix, respectively. The red circle represents the newly formed precipitates.

employing systematic experimental characterizations and analysis. Section 2 details the materials and methods, Section 3 provides results, Section 4 presents discussion, and Section 5 concludes the study. The present study offers insights into the effects of Ti addition and post-heat treatment on tuning microstructure and mechanical properties of cold spray additive manufactured bulk CoCeFeNi-based HEAs and provides important information that would help the development of cold spray additive manufacturing in the fabrication and applications of HEAs.

2. Materials and methods

2.1. Characterizations of the feedstock powders

The feedstock powders were prepared by mechanically mixing near-equiatomic CoCrFeNi powders (Jiangyin Dianyu New Materials Technology Co., Ltd., Jiangyin, China) with a nominal particle size in the range of 15–45 μm and Ti powders (Changsha Tijo Metal Materials Co., Ltd., Changsha, China) with a nominal powder size distribution ranging

from 15 to 53 μm. Both types of powders were produced by gas atomization with a purity larger than 99.9 %. The size and sphericity of these powders were characterized by a multifunctional particle size and shape analysis system (Camsizer X2, Leich, Germany). Fig. 1a–c and 1d–f present the morphologies and size distributions of the CoCrFeNi and Ti powders, respectively. It can be seen that both powders possess good sphericity with very few satellite powders, with the sphericity measured to be 83.39 % and 88.12 % for the CoCrFeNi and Ti powders, respectively. As shown in Fig. 1b, the CoCrFeNi powders possess cellular grains. The mean particle size of Ti powders (51.17 μm, Fig. 1f) is larger than that of CoCrFeNi powders (46.14 μm, Fig. 1c).

2.2. Fabrications of the bulk $(CoCrFeNi)_{1-x} + Ti_x$ HEAs

A Plasma Giken PCS-1000 system was employed for the cold spray additive manufacturing, during which highly compressed gas propelled the mixed powders to impact an aluminum substrate to form the bulk HEAs. The schematic diagram of the cold spray is depicted in Fig. 2a. A

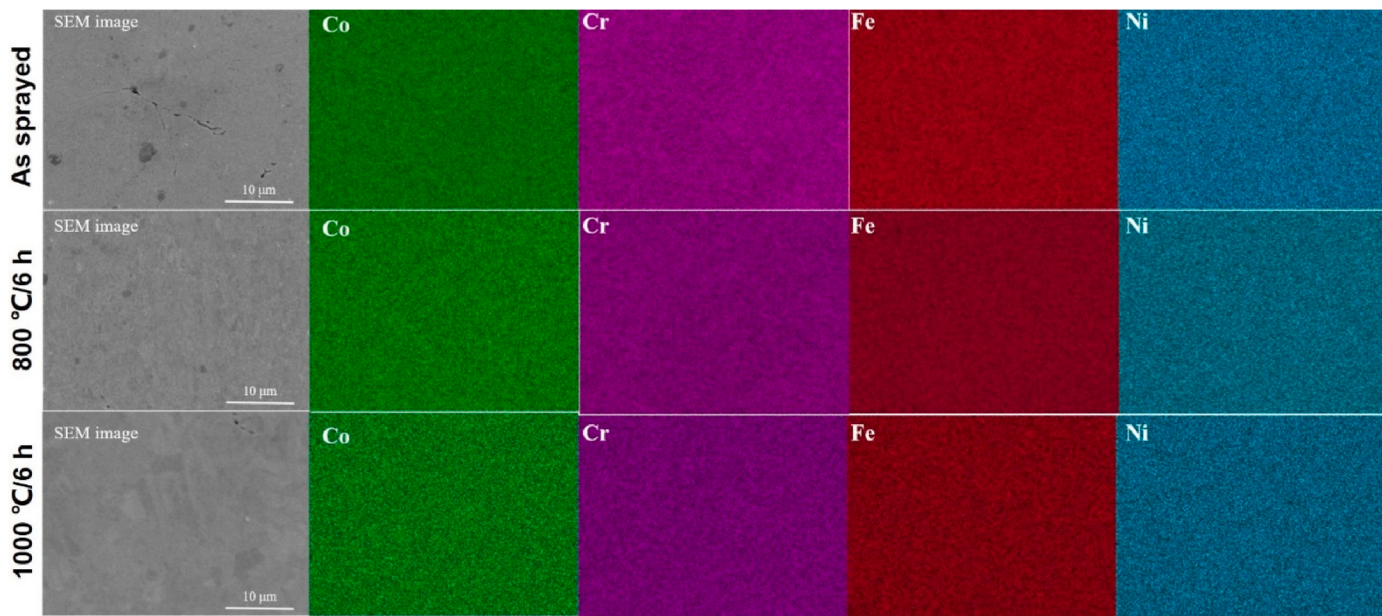


Fig. 5. EDS mapping results of the bulk CoCrFeNi HEAs under as sprayed, 800 °C/6 h and 1000 °C/6 h conditions.

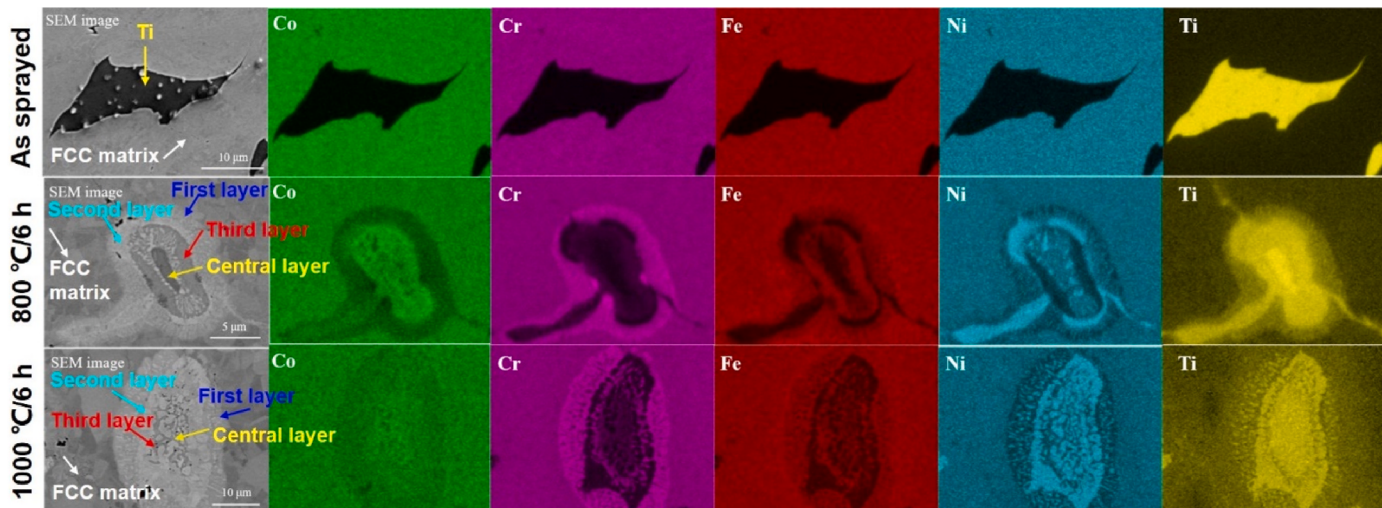


Fig. 6. EDS mapping results of the bulk CoCrFeNi + 4 at% Ti HEAs under as sprayed, 800 °C/6 h and 1000 °C/6 h conditions.

tungsten carbide nozzle was used with the throat diameter, outlet diameter, and expansion section length being 2.8 mm, 10 mm, and 20 cm, respectively. The powder feeding rate, robot speed, and step size were 8 r/min, 300 mm/s, and 1 mm, respectively. The propulsive gas was nitrogen, and the inlet pressure and temperature were 5 MPa and 850 °C, respectively. By this means, (CoCrFeNi)_{1-x} + Ti_x (x = 0, 4, and 7 at%) bulk HEAs with a size of 100 mm × 100 mm × 4 mm were fabricated on the aluminum substrates (Fig. 2b), which were removed by a reciprocating wire electrical discharge machining (wire EDM, DK7725C, BMW3000). Note that for convenience of notation, the fabricated bulk HEAs will be denoted as CoCrFeNi, CoCrFeNi + 4 at% Ti, and CoCrFeNi + 7 at% Ti or Ti₀, Ti₄, and Ti₇ across the manuscript. Subsequently, the bulk HEAs were made into small pieces of 8 mm × 4 mm × 4 mm (Fig. 2c) for microstructure characterizations and hardness and elastic modulus tests. Some of these samples after grinding off the oxide layer were also heat treated in an argon atmosphere at 800 °C for 6 h and 1000 °C for 6 h (denoted as 800 °C/6 h and 1000 °C/6 h hereafter), respectively, followed by cooling in water. The specific post-heat treatment parameters are shown in Table 1. In addition, room-

temperature tensile samples (Fig. 2d) were also prepared from the bulk HEAs. Note that two repeated tensile tests were conducted for each test condition.

The post-heat treatment temperatures of 800 and 1000 °C were determined based on thermodynamic calculations. The equilibrium phases of the bulk HEAs were calculated by Thermo-Calc using the TCNI9 database, the results of which are plotted in Fig. 3. It can be seen that CoCrFeNi remains a single FCC phase in the temperature range from 600 to 1300 °C (Fig. 3a). With the addition of Ti, the equilibrium phases contain η -Ni₃Ti, σ , and ordered phases (Fig. 3b,c), which confirm the feasibility of introducing phase engineering by mixing Ti with CoCrFeNi powders and post-heat treatment. Temperatures of 800 and 1000 °C were selected to introduce appropriate numbers of phases into the bulk HEAs to examine the effects of precipitate strengthening while avoiding excessive complexities.

2.3. Characterizations of microstructures of the bulk HEAs

X-ray diffractometer (XRD, MiniFlex600, Rigaku) along with post-

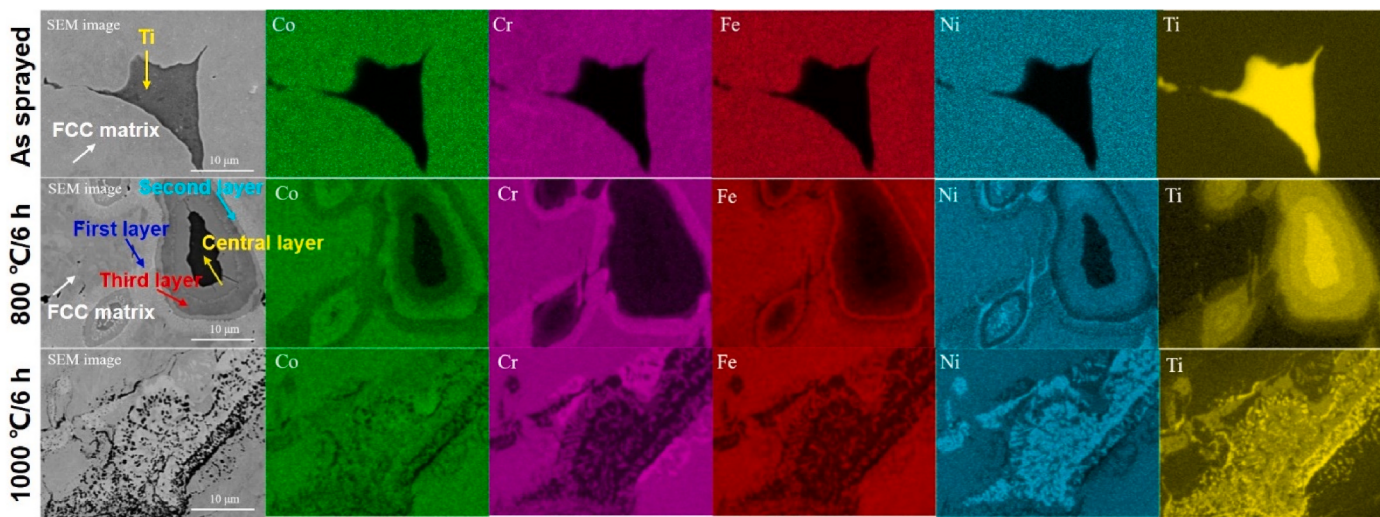


Fig. 7. EDS mapping results of the bulk CoCrFeNi + 7 at% Ti HEAs under as sprayed, 800 °C/6 h and 1000 °C/6 h conditions.

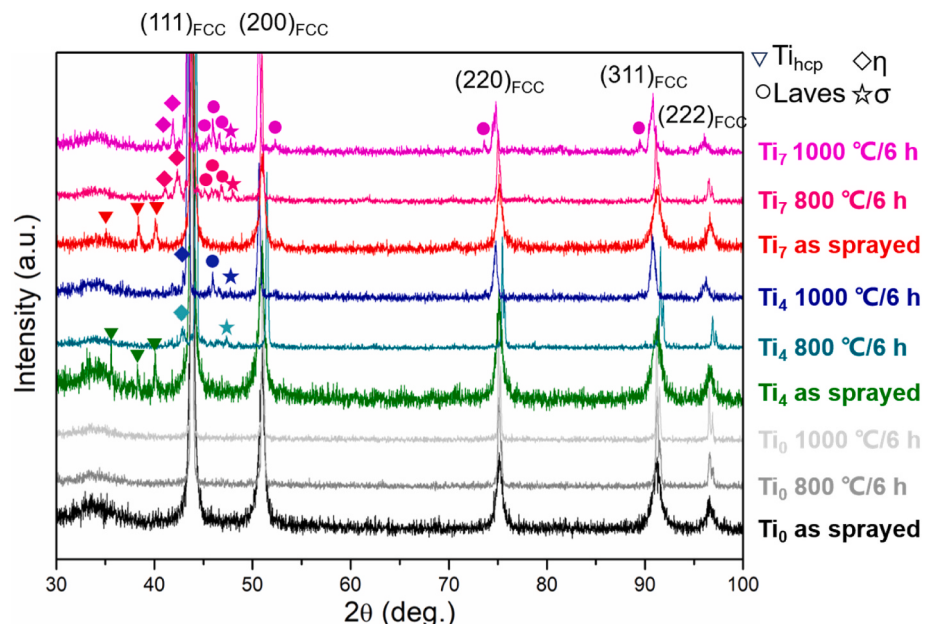


Fig. 8. XRD patterns of bulk HEAs of Ti_0 (i.e., CoCrFeNi), Ti_4 (i.e., CoCrFeNi + 4 at% Ti), and Ti_7 (i.e., CoCrFeNi + 7 at% Ti) under as sprayed, 800 °C/6 h, and 1000 °C/6 h conditions.

processing software MDI Jade 6 were employed to analyze the crystal structure and phases. The controlling parameters for the XRD experiment included 30–100° for the scanning range, 0.02° for the scanning step, 2°/min for the scanning speed, 40 kV for the tube voltage, and 15 mA for the tube current.

The optical microscope (OM, MIT300, Chongqing Aote Optical Instrument Co., Ltd.) was used to observe the microstructures of different samples, including the distributions and morphologies of Ti in CoCrFeNi matrix under different post-heat treatment conditions and the contents of Ti additions. A focused ion beam scanning electron microscopy (FIB-SEM, AMBER, TESCAN) equipped with an electron backscatter diffraction (EBSD) probe and an energy dispersive spectroscopy (EDS) probe was used for the characterization of grain orientations, precipitated phases, and element distributions. It is worth mentioning that after the conventional grinding and polishing, the EBSD sample was electro-polished in an electrolyte with a ratio of 20 mL H_2SO_4 and 80 mL CH_3OH (10–18 V voltage, 3 s).

To clarify the fracture mechanism after the uniaxial tensile tests, the fracture morphologies and microstructures of each tensile sample were investigated by tungsten filament scanning electron microscope (VEGA, TESCAN, OXFORD) and FIB-SEM. The detailed phases and possible phase changes of the bulk HEAs before and after the tensile experiment were studied by synchrotron X-ray diffraction with the beam energy of 60 keV ($\lambda = 0.020667 \text{ nm}$) at the beamline 3W1, Beijing Synchrotron Radiation Facility.

2.4. Measurements of mechanical properties of the bulk HEAs

The Vickers hardness and elastic modulus of the fabricated bulk HEAs were measured by a micron mechanical test system (CM500, NANOVE, Anton Paar, KLA). Each sample was examined with 4 × 5 points at an interval of 0.12 mm under the condition that the load, loading rate, and unloading rate were 1 N, 2 N/min, and 2 N/min, respectively. The room-temperature tensile stress-strain curves of the

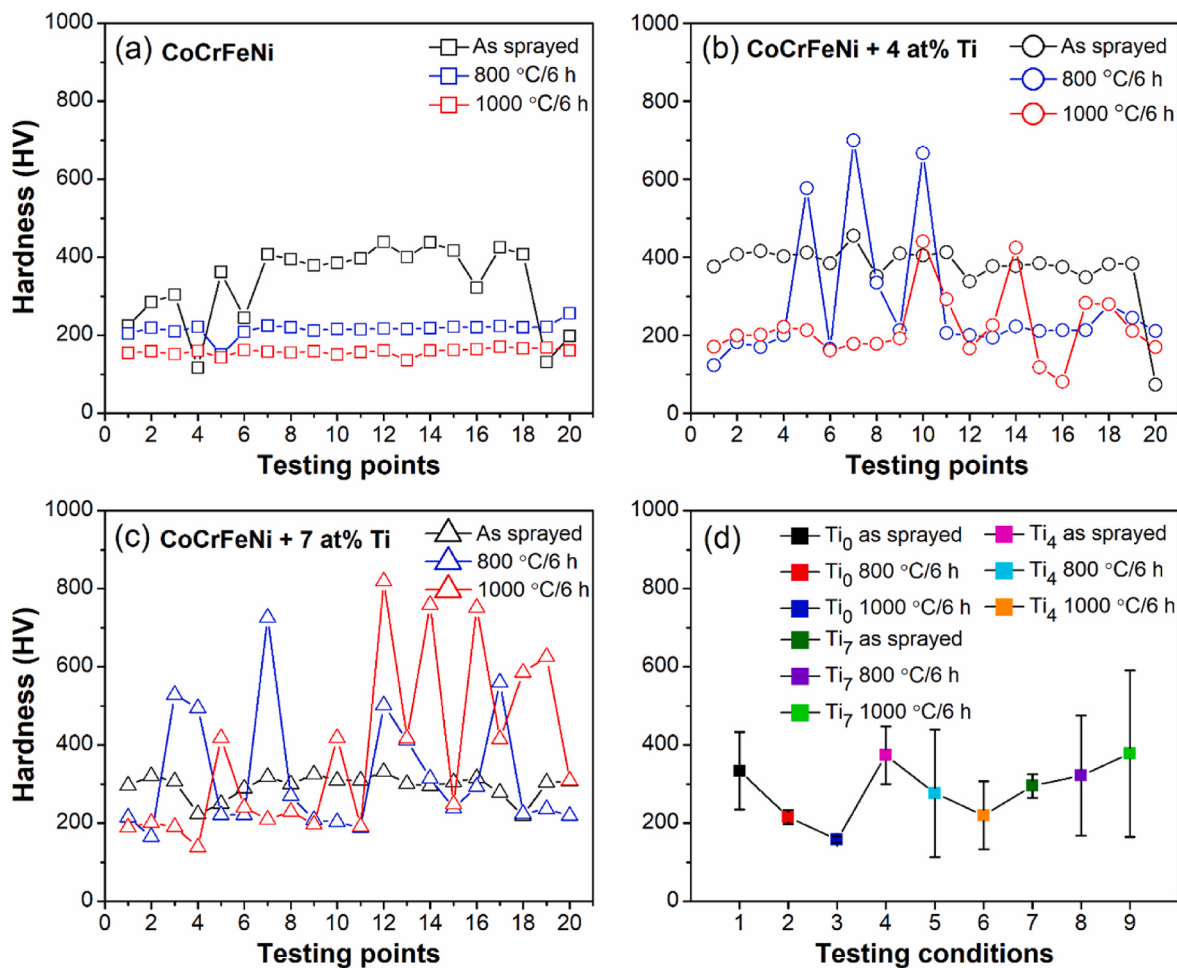


Fig. 9. Vickers hardness of the bulk HEAs in (a) CoCrFeNi, (b) CoCrFeNi + 4 at% Ti, and (c) CoCrFeNi + 7 at% Ti obtained by testing 20 indentation points of each sample. (d) Summarizes the average hardness and standard deviation of different testing conditions.

samples were tested on a 10 T mechanical testing machine (CMT5105, Shenzhen Sansi).

3. Results

3.1. Microstructure analysis

The optical micrographs with low and high magnifications of the bulk HEAs are shown in Fig. 4. The as sprayed CoCrFeNi is relatively dense with the presence of a small number of micro-holes (Fig. 4a). At high magnification, a small amount of the discontinuous original particle interface can be seen (Fig. 4d). For the as sprayed CoCrFeNi + 4 at% Ti (Fig. 4b) and CoCrFeNi + 7 at% Ti (Fig. 4c), the alloys are denser than the as sprayed CoCrFeNi. This can be ascribed to the mixing powder effect from the hard Ti powders on the improvement of the densification and bonding [48]. In addition, it is observed that severely deformed Ti powders (Fig. 4ef) relatively uniformly disperse in the CoCrFeNi matrix (Fig. 4bc).

After the 800 °C/6 h post-heat treatment, a few micropores appear in all three types of bulk HEAs (Fig. 4g–i), while the number of micropores is still less with the increase of Ti content, which again demonstrates the effect of Ti on assisting depositing [49]. The prior particle boundary (Fig. 4j–l) decreases owing to the high temperature-assisted atomic diffusion at the edge of particle interfaces and the microscopically tightly squeezed interfaces are proved easier to disappear [50]. This is consistent with previous studies, where metallurgical bonding can be formed at the particle interface through atomic diffusion and

recrystallization during the heat treatment process [50]. Particularly, for the dense bulk alloys, the particle interface gradually merges and disappears, which significantly weakens or eliminates the microstructure anisotropy from cold spray [50–52]. Notably, for the CoCrFeNi + 4 at% Ti (Fig. 4k) and CoCrFeNi + 7 at% Ti (Fig. 4l) alloys, the Ti powders exhibit gradient diffusion morphologies. Moreover, the dispersed small-sized precipitated phase can be seen in some light gray areas near the distorted Ti powders (Fig. 4kl), which illustrates that the Ti element has diffused around at this temperature, and even interacts with other elements (Co, Cr, Fe, Ni) to form some new precipitates or intermetallic compound.

After the 1000 °C/6 h post heat treatment, the number and severity of the micropores of the three alloys (Fig. 4m–o) decrease compared with those heat treated under 800 °C/6 h. At 1000 °C, the overall microstructure proves still relatively very dense (Fig. 4m–o). Additionally, the deformed Ti powders are hardly observed except at high magnifications (Fig. 4r). The precipitates around Ti also become invisible under OM, indicating that Ti powders have nearly finished diffusion into the CoCrFeNi matrix.

Figs. 5–7 show the EDS mapping results of the three types of bulk HEAs together with the original SEM morphologies under as sprayed, 800 °C/6 h, and 1000 °C/6 h conditions. For the CoCrFeNi HEAs (Fig. 5), regardless of whether the heat treatment is conducted, the distribution of elements proves not very uniform. For example, the element concentrations are Cr = 26.3 at%, Fe = 24.9 at%, Co = 24.6 at%, and Ni = 24.1 at% under the 1000 °C/6 h condition. Evenly distributed small-scale cluster sites of element segregation can be subtly observed,

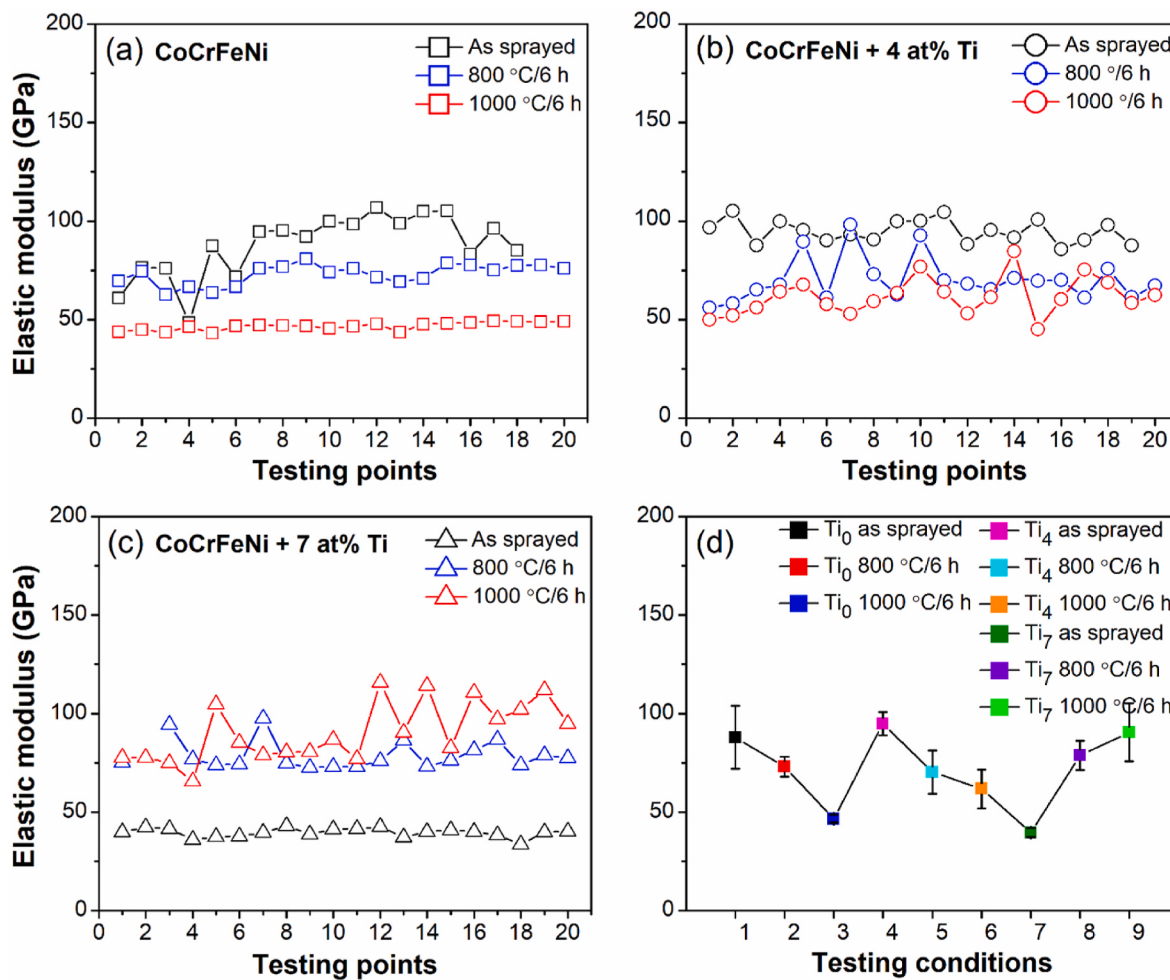


Fig. 10. Elastic modulus of bulk HEAs in (a) CoCrFeNi, (b) CoCrFeNi + 4 at% Ti, and (c) CoCrFeNi + 7 at% Ti obtained by testing 20 indentation points of each sample. (d) Summarizes the average hardness and standard deviation of different testing conditions.

which might be due to the formation of fine precipitates (Cr-rich σ phase) or element segregation at ultrafine grain boundaries caused by cold spray, which is in agreement with the previous study [53].

For the as sprayed CoCrFeNi + 4 at% Ti alloy (Fig. 6), strongly distorted Ti powder is found to embed into the CoCrFeNi matrix due to the supersonic impact, and the distribution of the Co, Cr, Fe, and Ni elements exhibits insignificant variation, which demonstrates that elements hardly diffuse at the absence of post-heat treatment. Under 800 °C/6 h post-heat treatment, small-sized precipitates with needle-like, granular, and agglomerated shapes form around the Ti powder. In addition, a small amount of Fe-rich region below 1 μm is observed within this region. Examining the mixed phase region outward toward inward, the first layer (the second row in Fig. 6) contains needle-like (Ni, Ti)-rich precipitates that are doped in the large Cr-rich precipitate, followed by a small amount of Fe. The second layer is comprised of a Ni-rich phase, and the Ti content is increased compared with the first layer. The third layer is rich in Fe and Ti and a discretely distributed mixed phase of Co-rich strip and Ni-rich block are observed. The central layer has a high concentration of Ti and poor of Cr and Fe. There exists pronounced composition segregation of the five elements in the whole alloy. Under 1000 °C/6 h, the distribution of the Co element becomes more uniform. The first layer mainly consists of (Cr, Fe)-rich phase, and a small amount of (Ni, Ti)-rich phase changes from needle-like to pestle-like and dopes in between. The second layer is a (Ni, Ti)-rich phase accumulation area and the Cr and Fe contents are nearly negligible. The third layer mainly contains the (Cr, Fe) phase and is doped with some (Ni, Ti) phase. The central layer has a structure of alternating

distributions of (Cr, Fe) and (Ni, Ti) phases.

Similar to the CoCrFeNi + 4 at% Ti HEAs, there is still nearly no diffusion in the as-sprayed CoCrFeNi + 7 at% Ti alloy (Fig. 7). After 800 °C/6 h heat treatment, the precipitates in the whole Ti powder are distributed in a closed-loop structure. Identically, the first layer exhibits a (Cr, Fe) rich structure distributed among needle-like (Ti, Ni) rich precipitate. The second layer enriches (Ti, Fe) elements. The third layer is rich in Co and Ti. The closer it is to the center layer, the higher the concentration of Ti element and the lower content of Cr element. When heat treated under 1000 °C/6 h, the closed-loop distribution characteristics of the phase disappear. There is no obvious segregation of Co in the whole large Ti powder, and the (Cr, Fe) rich-, (Ni, Ti) rich-, and pure Ti structures are mixed and distributed.

To further explore the possible phases in the HEAs, XRD results of the bulk HEAs under different conditions are shown in Fig. 8. It is seen that the bulk CoCrFeNi HEAs maintain a stable single FCC structure regardless of whether they undergo post-heat treatment. With the increase of heat treatment temperature, the XRD peaks become higher and narrower, indicating that the crystalline phase content increases and the grains grow with the increase in temperature.

For both the as sprayed CoCrFeNi + 4 at% Ti and CoCrFeNi + 7 at% Ti, only the peaks representing the HCP structure appear, which again confirms that the dark region (Fig. 4ef) is distorted Ti_{HCP} powders. For both cases under 800 °C/6 h and 1000 °C/6 h post-heat treatment, the characteristic peaks, including (Fe, Co)₂Ti-Laves, Ni₃Ti- η , and (Fe, Cr)- σ , are observed to varying degrees, consistent with a variety of precipitated phases shown in the SEM images of Figs. 6–7. Significantly, the amount

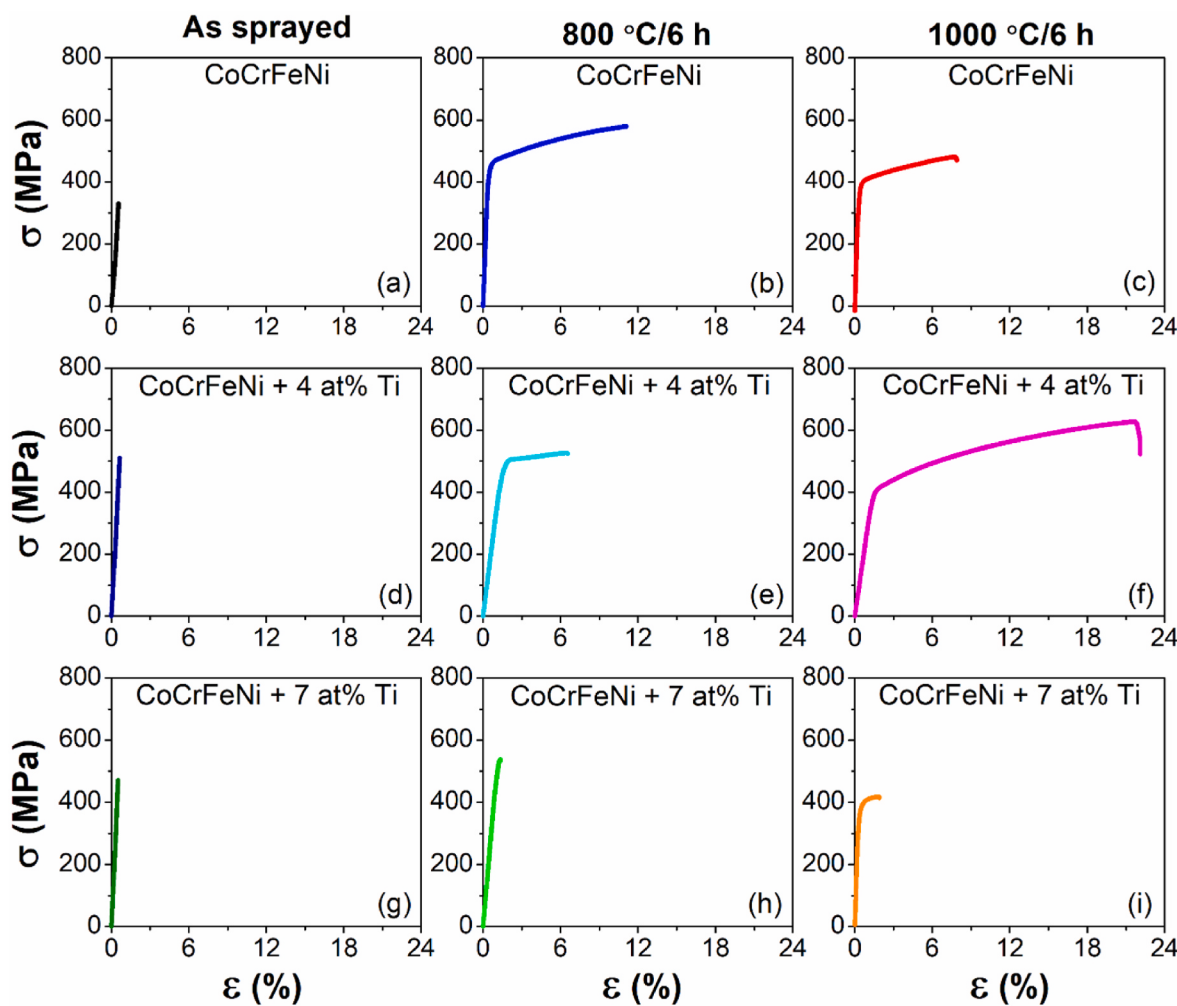


Fig. 11. Room-temperature uniaxial stress-strain curves of the bulk HEAs in (a–c) CoCrFeNi, (d–f) CoCrFeNi + 4 at% Ti, and (g–i) CoCrFeNi + 7 at% Ti under as sprayed, 800 °C/6 h, and 1000 °C/6 h conditions.

of $(\text{Fe}, \text{Co})_2\text{Ti}$ -Laves, Ni_3Ti - η , and (Fe, Cr) - σ that are classified as brittle intermetallic compound phases in CoCrFeNi + 4 at% Ti is less than those of CoCrFeNi + 7 at% Ti, and the phases grow with the increase in temperature. In addition, the main peaks of CoCrFeNi mixed with Ti all shift to the left to different extents, which is affected by the Ti content and temperature. This phenomenon is due to the diffusion of the large atomic size of the Ti elements into the CoCrFeNi matrix, resulting in local lattice distortion and the increase of lattice constant. Stein et al. [54] reported that various Laves phases can be effectively used as high-temperature strengthening precipitates to enhance high-temperature performance and stability. Previous studies [55,56] also reported that an appropriate amount of σ and η phase can improve the properties of the alloys, but the excessive amount can exert a detrimental effect on properties. Therefore, by cold spraying mixed CoCrFeNi and Ti powders and post-heat treatment, the microstructures and subsequently the properties of the bulk HEAs can be tuned.

3.2. Hardness, elastic modulus, and tensile properties

The Vickers hardness of the 20 testing points and their averages and standard deviations for the bulk HEAs under different conditions are plotted in Fig. 9a–c and 9d, respectively. For the CoCrFeNi alloy (Fig. 9a), the hardness values across different locations exhibit variations, which reflects on the structural inhomogeneity of the cold spray additive manufactured alloys. After post-heat treatment, the degree of hardness variations has greatly reduced and decreased with the increase

of heat treatment temperature by promoting interface diffusion and interface bonding to fill the ultra-fine gap [50]. Overall, the hardness value decreases with including heat treatment and the increase of temperature, which is expected as the strain and strain rate hardening in the as sprayed alloy are alleviated after post-heat treatment. A comparison of the hardness of the three conditions can be further seen in Fig. 9d, where the average hardness decreases with the increase of temperature due to thermal softening and the standard deviation is the largest for the as sprayed alloy.

The hardness results of CoCrFeNi + 4 at% Ti are shown in Fig. 9b. Similar to the CoCrFeNi case, the hardness of the as sprayed state is higher than those with post-heat treatment and decreases with the increase in temperature. However, the average hardness of CoCrFeNi + 4 at% Ti under all three conditions increases a bit than that of CoCrFeNi (Fig. 9d). This can be attributed to the existence of the HCP-Ti powders with higher hardness than the CoCrFeNi matrix and thus the mixing powder effects on increasing the working hardening of the fabricated alloys. In addition, it is observed that the hardness fluctuation of the CoCrFeNi + 4 at% Ti alloy in the as sprayed state is far less than those after heat treatment, which can be attributed to the various precipitates formed in the CoCrFeNi + 4 at% Ti deposit under post-heat treatment. The precipitates result in the alloy with regions of high hardness despite being exposed to the situation of recrystallization and grain growth. Compared with 800 °C, the deviation at 1000 °C is reduced due to more uniform diffusion and grain growth.

Contrary to the above two cases, the average hardness of the

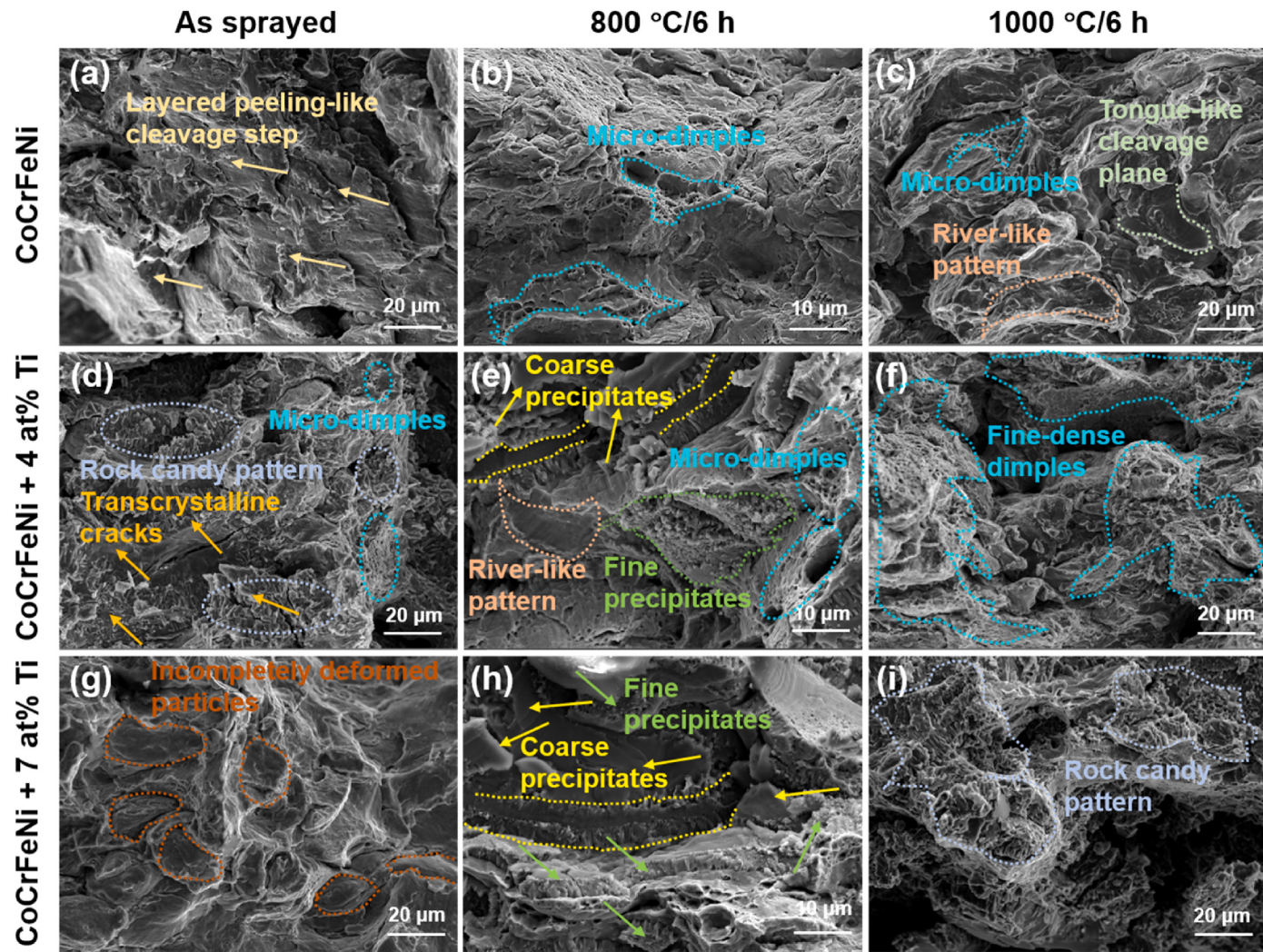


Fig. 12. SEM images of fractured morphologies of the bulk HEAs in (a–c) CoCrFeNi, (d–f) CoCrFeNi + 4 at% Ti, and (g–i) CoCrFeNi + 7 at% Ti for as sprayed, 800 °C/6 h, and 1000 °C/6 h conditions.

CoCrFeNi + 7 at% Ti alloy increases with the increase of post-heat treatment temperature, as shown in Fig. 9d. The point-to-point hardness exhibits wild fluctuations for the 800 °C/6 h and 1000 °C/6 h conditions, where the largest and smallest values are ~850 and ~100 HV, respectively (Fig. 9c). The increase of hardness with the increase in temperature is because the increase of Ti content leads to the formation of a variety of precipitates and intermetallic compounds, the precipitation strengthening of which dominates over the high-temperature softening. In addition, the coexistence of CoCrFeNi, gradient Ti, and a variety of precipitates facilitated by the Ti concentration gradients results in quite inhomogeneous microstructures and might account for the large variations of the hardness for CoCrFeNi + 7 at% Ti under post-heat treatment. It is also noted that the fluctuation and average hardness of the as sprayed CoCrFeNi + 7 at% Ti are less than those of CoCrFeNi and CoCrFeNi + 4 at% Ti. This is partly due to the mixing of hard Ti powders during cold spray to make the microstructure denser [48]. It's noted that with the addition of 7 at% Ti, the average alloy's hardness is less than the other two types of alloys in the as sprayed state. This behavior might be due to the weak cohesion of the excessive Ti powders within the CoCrFeNi matrix.

As the literature has shown that the hardness and elastic modulus are related to the plastic and wear resistance properties of the material [57], the elastic modulus of the bulk HEAs under the three conditions is analyzed in Fig. 10. Overall, it can be seen that the elastic modulus of the

three types of bulk alloys follows a similar trend to their hardness except that the degree of fluctuation is decreased, which indicates that the cohesion of the alloys is relatively good. Such temperature and structure dependence of the elastic modulus is consistent with previous studies [58,59]. Overall, the addition of 4 at% Ti can yield a higher elastic modulus with a smaller deviation than the as sprayed and 7 at% Ti addition states, which is associated with the appropriate amounts of precipitates generated after post-heat treatment, grain recrystallization, and mixing powder effect from the hard Ti powders. It is worth noting the elastic modulus with the 7 at% Ti addition is the lowest among the alloys, which might be due to that the excessive addition of Ti results in weak cohesion of the alloy. As the elastic modulus macroscopically reflects the ability of the material to resist elastic deformation, and mesoscopically reflects the bonding force between particles, introducing Ti particles and post-heat treatment can tune the elastic properties of the bulk CoCrFeNi alloy, thus helping achieve strength and ductility synergy.

The uniaxial tensile stress-strain curves of the bulk HEAs are shown in Fig. 11. It is obvious that the as sprayed HEAs with and without the addition of Ti powders (Fig. 11a, 11d, and 11g) possess quite poor ductility with fracture strain less than 1 %. The brittleness reflects the strong working hardening and the existence of weakly bonded particles of the cold spray manufacturing process. After including the Ti powders, it is seen that the ultimate tensile strength (UTS) of the as sprayed bulk

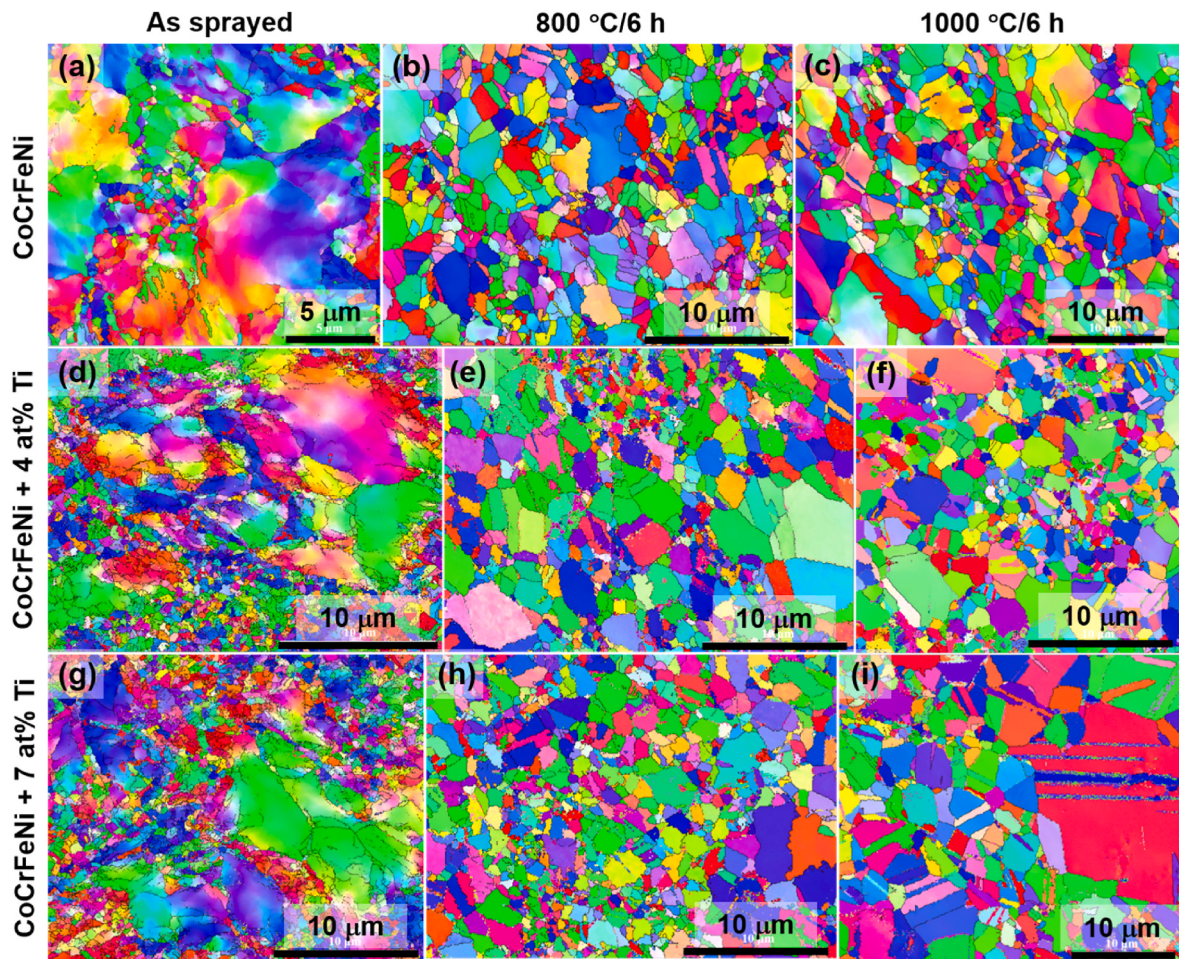


Fig. 13. IPF maps near the fracture location of the tensile deformed bulk alloys in (a–c) CoCrFeNi, (d–f) CoCrFeNi + 4 at% Ti, and (g–i) CoCrFeNi + 7 at% Ti for as sprayed, 800 °C/6 h, and 1000 °C/6 h conditions.

HEAs (510.60 MPa for CoCrFeNi + 4 at% Ti in Figs. 11d and 471.33 MPa for CoCrFeNi + 7 at% Ti in Fig. 11g) increases a bit comparing with CoCrFeNi (330.45 MPa, Fig. 11a), which can be attributed to the mixing powder effect by adding the hard Ti powders.

After post-heat treatment at 800 °C/6 h, the UTS and elongation to fracture of all three types of alloys increase (Fig. 11b, 11e, and 11h), among which the CoCrFeNi alloy has the best strength and ductility (579.68 MPa and 11.10 %, respectively), followed by CoCrFeNi + 4 at% Ti (523.98 MPa and 6.55 %, respectively) and CoCrFeNi + 7 at% Ti (534.28 MPa and 1.35 %, respectively). These results are consistent with Yu et al.'s study [60], where heat treatment can promote recrystallization and growth of grains at the particle interface to enhance the bonding of cold sprayed alloy, help the formation of dimples and crack passivation, and hinder the expansion of cracks, thus improving strength and ductility. As the temperature as high as 800 °C is conducive to more uniform atomic diffusion at the particle interface, static recrystallization and grain growth could occur in particle boundary, which help to generate metallurgical bonding and form dimples in the CoCrFeNi alloy (Fig. 11b). The reason for the poor ductility of Ti-containing alloys (Fig. 11e and 11h) could be attributed to the variety of precipitates generated in the diffusion zone centered on Ti particles, particularly for the CoCrFeNi + 7 at% Ti, which makes the overall microstructure heterogeneous and more prone to crack initiation. In addition, element segregation accounts for the increase in strength of the Ti-containing alloys.

Comparing the alloys at 1000 °C/6 h with those at 800 °C/6 h, both the UTS and elongation to fracture of the CoCrFeNi alloy decrease to

480.83 MPa and 7.90 %, respectively, while the UTS (417.78 MPa) decreases and elongation to fracture (1.90 %) slightly increases for the CoCrFeNi + 7 at% Ti alloy. The decrease in UTS with the increase in temperature is expected as the thermal softening effect on the work-hardened alloy. The decrease in ductility of the CoCrFeNi alloy may be accounted for by the agglomeration of the micropores under higher temperatures. While the increase in ductility of the CoCrFeNi + 7 at% Ti may be due to the homogeneity of the microstructure. Interestingly, the UTS (626.71 MPa) and ductility (22.10 %) of the CoCrFeNi + 4 at% Ti alloy exhibit good strength and ductility synergy in comparison with the bulk HEAs under the other conditions. This can be attributed to the full diffusion of the 4 at% Ti elements and the dissolution of unstable phases at 1000 °C/6 h.

3.3. Microscopic interpretation of the deformation mechanisms

Fig. 12 shows the tensile fracture morphologies of the bulk HEAs under different conditions. The as sprayed bulk HEAs with or without the addition of Ti powders exhibit characteristics of brittle fracture. Specifically, CoCrFeNi shows a layered peeling-like cleavage step resulting from weak adhesion among deformed particles (Fig. 12a). Rock candy pattern, transcrystalline crack, and micro-dimples are observed in the CoCrFeNi + 4 at% Ti alloy, which demonstrate Ti enhances grain boundary strength, and thus intergranular fracture transits to transgranular fracture (Fig. 12d). For CoCrFeNi + 7 at% Ti, incompletely deformed Ti particles and the associated particle boundaries exist, which indicate that the amount of Ti added could not be fully

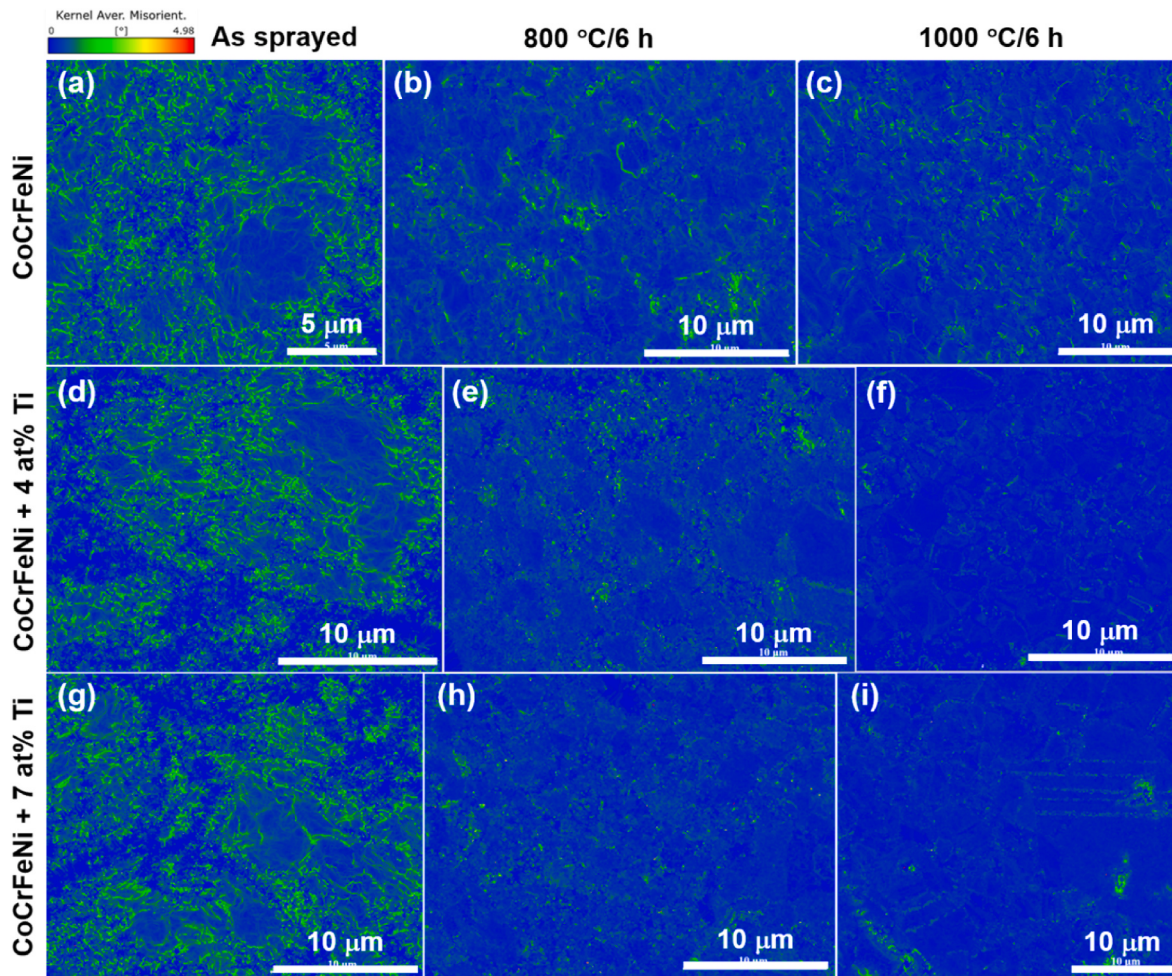


Fig. 14. KAM maps near the fracture location of the tensile deformed bulk alloys in (a–c) CoCrFeNi, (d–f) CoCrFeNi + 4 at% Ti, and (g–i) CoCrFeNi + 7 at% Ti for as-sprayed, 800 °C/6 h, and 1000 °C/6 h conditions.

plastically deformed, resulting in the embedding of particles into the CoCrFeNi matrix. When subjected to external loading, the crack could rapidly propagate along the particle boundary (Fig. 12g).

After post-heat treatment at 800 °C/6 h, the fracture morphology of CoCrFeNi (Fig. 12b) exhibits micro-dimples, tearing ridges, and blunted cracks, indicating that the heat treatment promotes bonding strength and ductility of the bulk alloy by the fusion of the particle interface. For CoCrFeNi + 4 at% Ti (Fig. 12e), it is brittle with crack propagation along the coarse precipitates with sizes of tens of microns. However, it is also noted the emergence of abundant fine precipitates might help suppress the brittle failure process. For the CoCrFeNi + 7 at% Ti alloy, brittle failure originates from the coarse-striped brittle phase due to an excess of Ti and remaining particle boundaries (Fig. 12h).

After post-heat treatment at 1000 °C/6 h, tongue-like cleavage plane, river-like pattern and interspersed micropores in CoCrFeNi are typical quasi-cleavage fracture characteristics, which cause the plasticity inferior to 800 °C/6 h (Fig. 12c). The fracture morphology of CoCrFeNi + 4 at% Ti shows a large number of fine-dense dimples, indicating strong metallurgical bonding of the alloy. In addition, the coarse precipitates disappear and fine precipitates are present, contributing to the improvement of the strength and plasticity of the alloy (Fig. 12f). On the contrary, large amounts of rock candy pattern with a smooth exterior surface are present in the CoCrFeNi + 7 at% Ti alloy, which demonstrates the brittle fracture behavior of the alloy (Fig. 12i).

To clarify the effects of post-heat treatment temperature and Ti content, EBSD was performed to investigate grain microstructure through inverse polar figure (IPF) maps (Fig. 13), kernel average

misorientation (KAM) maps (Fig. 14), and distributions of grain sizes (Fig. 15).

As shown in Fig. 13, many deformed grains are observed in the as sprayed bulk (CoCrFeNi)_{1-x} + Ti_x HEAs (Fig. 13a, 13d, and 13g), which are mainly caused by the supersonic impact from the cold spray process. It is found that ultrafine grains (<1 μm) are distributed at the boundaries of micron-sized large grains. Therefore, the degree of deformation is highest at the grain boundary and decreases towards the grain interior. This result is consistent with the study of Chen et al. [30], who reported bimodal grain structure produced by the cold spray process. After post-heat treatment at 800 °C/6 h, static recovery and recrystallization occur (see Fig. 14 for more information), which makes the distributions of the grain size more uniform and the size of the grain larger than the as sprayed state. This phenomenon is consistent with Feng et al.'s study [34], which attributed the growth of ultrafine grains and equiaxed grains to static recrystallization. With the temperature further increased to 1000 °C, the grain sizes of the (CoCrFeNi)_{1-x} + Ti_x HEAs increase compared with those under 800 °C. As the increase in temperature can promote the growth of the recrystallized grains through grain boundary migration and mutual phagocytosis between grains, such results are expected, which are also consistent with the study of Feng et al. [34].

As the KAM map is closely related to geometrically necessary dislocations (GNDs) [61], it can be used to demonstrate the local plastic deformation of the alloys. Fig. 14 shows the KAM maps of the bulk alloys under different conditions with misorientation larger than 5° neglected during the KAM calculation. For the as sprayed alloys, the KAM maps indicate severe plastic deformation from the cold spray process

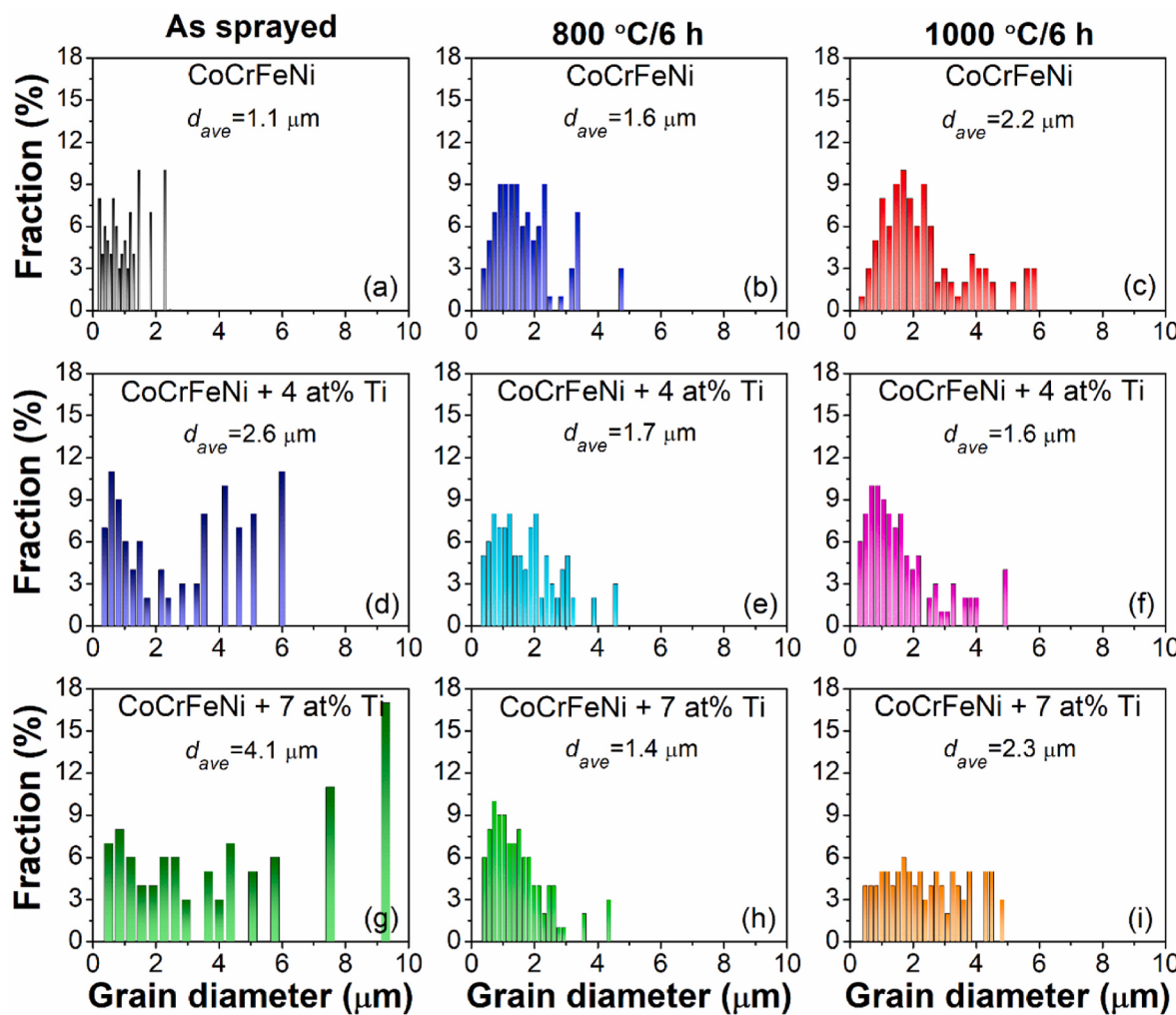


Fig. 15. Area-weighted fraction of grain sizes near the fracture location of the tensile deformed bulk alloys in (a–c) CoCrFeNi, (d–f) CoCrFeNi + 4 at% Ti, and (g–i) CoCrFeNi + 7 at% Ti for as sprayed, 800 °C/6 h, and 1000 °C/6 h conditions.

(Fig. 14a, 14d, and 14g). As the KAM values below 1.5° can be used to indicate recrystallization, it is seen that recovery and recrystallization increase for the $(\text{CoCrFeNi})_{1-x} + \text{Ti}_x$ alloys with the increase in heat treatment temperature. During static recovery, dislocation motions help release the strain energy generated during the cold spray process. Afterward, strain-free equiaxed grains with low dislocation densities nucleate and grow through static recrystallization. Due to static recovery and recrystallization, elongated grains in the as sprayed alloy are seen to disappear and fine grains nucleate at the grain boundaries [34].

The area-weighted fractions of grain sizes of the bulk alloys are shown in Fig. 15. For the CoCrFeNi alloy, the average grain sizes are 1.1, 1.6, and 2.2 μm for the as sprayed, 800 °C/6 h, and 1000 °C/6 h conditions, being consistent with the above analysis. On the contrary, after mixing with 4 and 7 at% Ti, the grain size decreases with the increase in post-heat treatment temperature. The average grain sizes are 2.6, 1.7, and 1.6 μm and 4.1, 1.4, and 2.3 μm for CoCrFeNi + 4 at% Ti and CoCrFeNi + 7 at% Ti, respectively. Therefore, this demonstrates that the addition of hard Ti is beneficial for grain refinement by mixing powder effect and by hindering atomic diffusion and grain boundary migration. It is observed that at 1000 °C/6 h, the CoCrFeNi + 4 at% Ti alloy still possesses fine grains, which may be due to the generated fine precipitates prohibiting the grain boundary migration, thus increasing the minimum recrystallization temperature. Note that for the CoCrFeNi + 7 at% Ti alloy, some grains grow abnormally into very coarse grains, which might be related to the severe and heterogeneous deformation

caused by excessive Ti during cold spray. In addition, a large number of annealing twins are observed that reflect the decrease of the stacking fault energy. Therefore, adding appropriate amounts of Ti (e.g., 4 at%) can help achieve strength and ductility synergy under post-heat treatment by yielding fine grains. However, an excessive amount of Ti (e.g., 7 at%) will lead to abnormally large grains and the formation of very coarse structures that are detrimental to mechanical properties.

Under the interplay between the content of Ti and post-heat treatment temperature, complex type, quantity, and size of the phases are formed. To confirm whether exist phase changes during the tensile test, high-precision synchrotron X-ray diffraction results are presented in Fig. 16. It is seen that the number and sites of peaks change insignificantly before and after the tensile test, indicating no phase change occurs after tensile deformation. Specifically, the bulk CoCrFeNi alloys with and without the addition of Ti powders remain a single FCC phase after cold spray, 800 °C/6 h and 1000 °C/6 h, and uniaxial tension. The peak width gradually narrows with the increase in post-heat treatment temperature as a result of the grain growth. On the contrary, multiple peaks have been revealed in the CoCrFeNi + 4 at% Ti and CoCrFeNi + 7 at% Ti alloys, which confirm the formation of precipitates by introducing Ti powders and post-heat treatment.

To clarify the formed precipitates in the Ti-containing HEAs under different conditions, the magnified Synchrotron X-ray diffraction results within the 4.5–10.5° is analyzed in Fig. 17. Overall, the precipitates are confirmed to be Fe_2Ti , Co_2Ti , CoTi_2 , CrFe , Ti_{BCC} , and Ni_3Ti . For the as

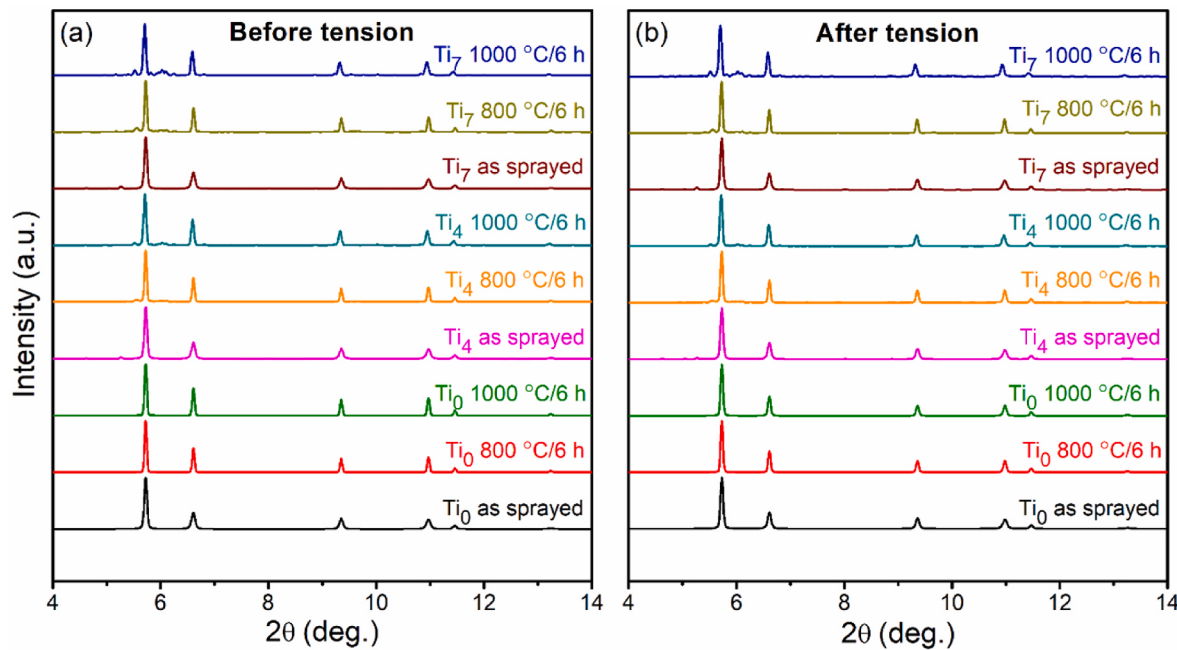


Fig. 16. Synchrotron X-ray diffraction patterns (4–14°) of bulk HEAs of Ti₀ (i.e., CoCrFeNi), Ti₄ (CoCrFeNi + 4 at% Ti), and Ti₇ (CoCrFeNi + 7 at% Ti) under as sprayed, 800 °C/6 h, and 1000 °C/6 h conditions in (a) before tension and (b) after tension.

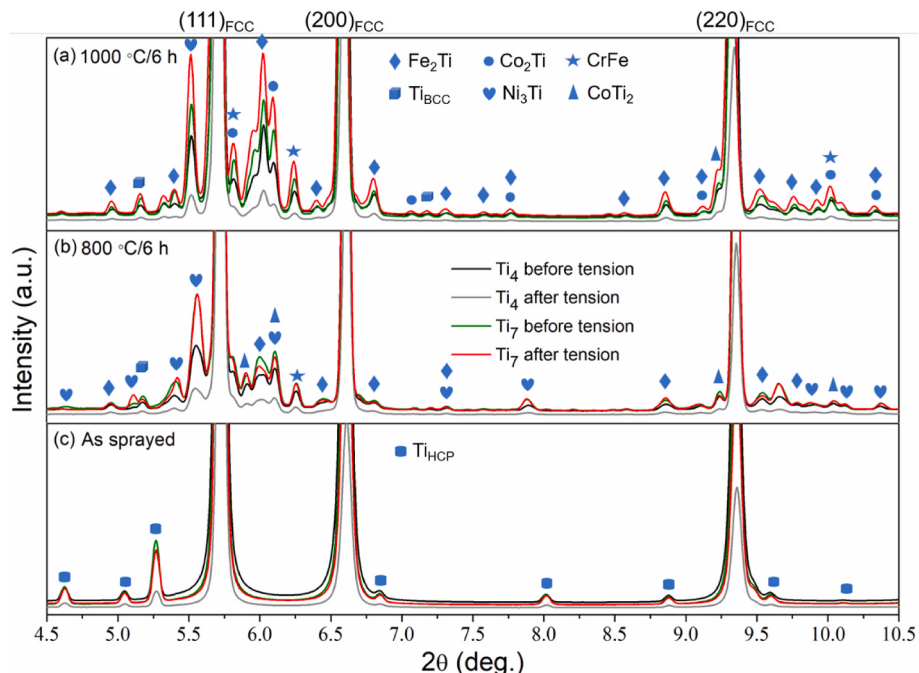


Fig. 17. Magnified synchrotron X-ray diffraction patterns (4.5–10.5°) of bulk HEAs of Ti₄ (CoCrFeNi + 4 at% Ti) and Ti₇ (CoCrFeNi + 7 at% Ti) under (a) 1000 °C/6 h, (b) 800 °C/6 h, and (c) as sprayed conditions before and after tension.

sprayed alloys, the HCP Ti and FCC CoCrFeNi coexist, being consistent with the previous XRD results in Fig. 8. Under 800 °C/6 h, intermetallic compound phases are formed due to atomic diffusion. The effect of tension lies in the peak intensity, where the peak intensity decreases for 4 at% addition of Ti and the opposite occurs for 7 at% addition of Ti after tension. As the CoCrFeNi + 4 at% Ti contains a small number of precipitates, deformation mainly occurs in the CoCrFeNi matrix during tension and the fine precipitates contribute to the improvement of the mechanical properties, resulting in the decrease in peak intensity. On the contrary, CoCrFeNi + 7 at% Ti contains too many coarsen

precipitates, which cause early fracture of the alloy. In addition, peak width decreases with the increase of post-heat treatment temperature, which is due to the grain growth. These results concur with the analysis above. For the CoCrFeNi + 4 at% Ti, a proper amount of the fine precipitates and fine grains provide a good balance between tensile strength and ductility. While the excessive brittle phases, especially Laves phases, in the CoCrFeNi + 7 at% Ti alloy deteriorate the tensile property.

4. Discussion

4.1. Comparison of mechanical properties with other manufacturing methods

Thanks to the strong work hardening effect from the cold spray process, the average hardness of the as sprayed bulk CoCrFeNi (333.7 HV) is higher than the microhardness of mechanically-alloyed CoCrFeNi (136 HV), CoCrFeNiAl (262 HV), and CoCrFeNiTi (269 HV) [62], laser cladding CoCrFeNi (200 HV) [63], and spark plasma sintering CoCrFeNi (150 HV) [64]. With the addition of 4 at% of Ti powders, the average hardness of the HEA can be further improved to 373.3 HV and the hardness has less fluctuation than the as sprayed state. In terms of elastic modulus, the values of the as sprayed CoCrFeNi and CoCrFeNi + 4 at% Ti are 87.9 ± 16.0 GPa and 94.8 ± 5.9 GPa, respectively. Compared with the experimentally measured elastic modulus of ~ 214 GPa for CoCrFeNi fabricated by vacuum induction melting [65], the elastic modulus of the cold spray fabricated alloy is rather low. Nevertheless, as the ratio of hardness to elastic modulus could be used to represent the ability to wear resistance [32], the above results hint that cold spray fabricated HEAs might be good candidates for wear-related applications.

Comparing the UTS and ductility of CoCrFeNi_x from cold spray with those of other manufacturing methods, it is revealed that the present results are generally comparable to powder-based manufacturing technologies but less than those from melting routes. For example, through in-situ laser powder bed fusion of CoCrFeNi and Ti powders, Li et al. [66] fabricated CoCrFeNi and CoCrFeNi_{Ti0.3} HEAs with UTS and elongation to failure being 649 MPa and 22.5 % and 905 MPa and 3.7 %, respectively. By vacuum hot pressing sintering process, Li et al. [67] reported the best UTS of CoCrFeNi and CoCrFeNi_{Ti1.0} to be 670 MPa and 783 MPa, respectively, and the UTS decreases with further increase of Ti content. While, the arc-melted and annealed CoCrFeNi_{Ti0.2} by Zhang et al. [68] had UTS and tensile elongation as high as ~ 1200 MPa and ~ 20 %, respectively. This is partly due to the cold spray processing parameters as well as the Ti content and post-heat treatment conditions were not optimized in the present study, and thus the best UTS and ductility were not achieved. It is also rooted in cold spray manufacturing technology, where defects, such as powder particle boundaries and micropores, are difficult to control in the resultant alloys. Nevertheless, with the introduction of mixed powders and post-heat treatment, the present study demonstrated that cold spray is a viable additive manufacturing method to fabricate bulk HEAs with tunable mechanical properties.

4.2. Limitations of the present study and future research

Besides the above analysis, there remain unanswered questions in the study, which are outlined below for future research. Firstly, as presented in Section 4.1, both the processing parameters of cold spray and the content of Ti powders and post-heat treatment conditions were not optimized in the study. Therefore, it lacks sufficient information to evaluate the effects of the cold spray process and the proposed property tuning approaches in fabricating CoCrFeNi-based HEAs. In the future, process optimizations will be performed to delimit the potentials of the cold spray as bulk HEAs additive manufacturing technology. Moreover, the dominant factors that contribute to the strength and ductility were not quantitatively analyzed. It is still not clear to what extent the dislocation, grain size, and precipitate contribute to the strengthening. In addition, the evolution of micropores during post-heat treatment was also not examined. Furthermore, atomic-scale high-resolution characterizations using a transmission electron microscope (TEM) are also necessary to elucidate the deformation mechanisms of the HEAs under the complex interplay of dislocations, precipitates, and grain boundaries within the highly heterogeneous microstructures. The above should be clarified to rationally tune the microstructure and properties. Finally, the potential applications of the HEAs that take advantage of the

characteristics of the cold spray process should be examined in the future.

5. Conclusions

In summary, the microstructure and mechanical properties of cold spray additive manufactured CoCrFeNi, CoCrFeNi + 4 at% Ti, and CoCrFeNi + 7 at% Ti bulk HEAs are studied, and the effects of Ti content and post-heat treatment of 800 °C/6 h and 1000 °C/6 h are clarified. Major conclusions are summarized below.

- (1) The bulk HEAs are relatively dense with few pores and original particle interfaces. Mixing powders helps densify the alloys. After post-heat treatment, the original particle interfaces disappear and the micropores are not noticeably increased.
- (2) Precipitates are formed in the Ti-containing HEAs. The precipitates are confirmed to be Fe₂Ti, Co₂Ti, CrFe, Ti_{BCC}, Ni₃Ti, and CoTi₂ based on high-precision synchrotron XRD. These precipitates are not found to be changed during uniaxial tension.
- (3) The hardness and elastic modulus of the as sprayed CoCrFeNi are 333.7 HV and 87.9 GPa, respectively, and in general, they increase with the increase in Ti content and vice versa with temperature for CoCrFeNi and CoCrFeNi + 4 at% Ti. However, the two properties are positively correlated with temperature for CoCrFeNi + 7 at% Ti due to the high temperature promoted formation of precipitates.
- (4) The as sprayed bulk alloys regardless of Ti added show high strength but low ductility owing to the high work hardening from the cold spray. After post-heat treatment, both the strength and ductility can be increased due to atomic diffusion-induced cohesion, the formation of fine precipitates, and the emergence of fine and relatively uniform grains from static recovery and recrystallization. The UTS and elongation to failure increase from 330.4 MPa to 0.54 %, respectively for the as sprayed CoCrFeNi to 626.7 MPa and 22.1 %, respectively for CoCrFeNi + 4 at% Ti after 1000 °C/6 h treatment.
- (5) Due to grain growth in CoCrFeNi and excessive flaky Laves, η , and σ phases and abnormally large grain in CoCrFeNi + 7 at% Ti, the tensile performance decreases after being treated at 1000 °C compared with 800 °C for these two alloys.

Declaration of competing interest

The authors declare the following financial interests/personal relationships which may be considered as potential competing interests:

Fanchao Meng reports financial support was provided by Natural Science Foundation of Shandong Province.

Acknowledgments

Fanchao Meng acknowledges financial support from the Natural Science Foundation of Shandong Province (ZR2021QE110). Shuying Chen is financially supported by the National Natural Science Foundation of China (Grant Nos. 52371163 and 52001271). Xin Chu is grateful for financial support from the Guangdong Academy of Sciences Special Fund for Comprehensive Industrial Technology Innovation Center Building (2022GDASZH-2022010107), GDAS' project of Science and Technology Development (2022GDASZH-2022010203-003), and Guangdong Special Support Program (2019BT02C629). Yang Tong acknowledges financial supports from the National Natural Science Foundation of China (Grant Nos. 52001272 and 52371164), Taishan Scholars Program of Shandong Province (tsqn202103052), Yantai city matching fund for Taishan Scholars Program of Shandong Province, and Top Discipline in Materials Science of Shandong Province.

References

- [1] Yeh J-W, Chen S-K, Lin S-J, Gan J-Y, Chin T-S, Shun T-T, et al. Nanostructured high-entropy alloys with multiple principal elements: novel alloy design concepts and outcomes. *Adv Eng Mater* 2004;6(5):299–303.
- [2] Tsai M-H, Yeh J-W. High-entropy alloys: a critical review. *Mater Res Lett* 2014;2(3):107–23.
- [3] Yeh J-W. Recent progress in high-entropy alloys. *Ann Chimie Sci Matériaux* 2006;31(6):633–48.
- [4] Wu Z, He M, Cao H, Wang S, Chen R, Cao B, et al. Ultrahigh-strength and ductile CoCrFeNi-based high-entropy alloys manufactured by laser powder bed fusion with multiple strengthening mechanisms. *J Mater Res Technol* 2023;25:2948–60.
- [5] Shahmir H, Mehranpour MS, Shams SAA, Langdon TG. Twenty years of the CoCrFeNiMn high-entropy alloy: achieving exceptional mechanical properties through microstructure engineering. *J Mater Res Technol* 2023;23:3362–423.
- [6] Gorr B, Schellert S, Müller F, Christ H-J, Kauffmann A, Heilmair M. Current status of research on the oxidation behavior of refractory high entropy alloys. *Adv Eng Mater* 2021;23(5):2001047.
- [7] Chen S, Qiao J, Diao H, Yang T, Poplawsky J, Li W, et al. Extraordinary creep resistance in a non-equiautomic high-entropy alloy from the optimum solid-solution strengthening and stress-assisted precipitation process. *Acta Mater* 2023;244:118600.
- [8] Chen S, Li W, Wang L, Yuan T, Tong Y, Tseng K-K, et al. Stress-controlled fatigue of HfNbTaTiZr high-entropy alloy and associated deformation and fracture mechanisms. *J Mater Sci Technol* 2022;114:191–205.
- [9] Sharma A, Oh MC, Ahn B. Microstructural evolution and mechanical properties of non-Cantor AlCuSiZnFe lightweight high entropy alloy processed by advanced powder metallurgy. *Mater Sci Eng, A* 2020;797:140066.
- [10] Chae MJ, Sharma A, Oh MC, Ahn B. Lightweight AlCuFeMnMgTi high entropy alloy with high strength-to-density ratio processed by powder metallurgy. *Met Mater Int* 2021;27:629–38.
- [11] Sharma A, Lee H, Ahn B. Effect of additive elements ($X = \text{Cr}, \text{Mn}, \text{Zn}, \text{Sn}$) on the phase evolution and thermodynamic complexity of AlCuSiFe-x high entropy alloys fabricated via powder metallurgy. *Met Mater Int* 2022;28:2216–24.
- [12] Wang X, Guo W, Fu Y. High-entropy alloys: emerging materials for advanced functional applications. *J Mater Chem A* 2021;9(2):663–701.
- [13] Pickering EJ, Carruthers AW, Barron PJ, Middleburgh SC, Armstrong DE, Gandy AS. High-entropy alloys for advanced nuclear applications. *Entropy* 2021;23(1):98.
- [14] Miracle DB, Miller JD, Senkov ON, Woodward C, Uchic MD, Tiley J. Exploration and development of high entropy alloys for structural applications. *Entropy* 2014;16(1):494–525.
- [15] Miracle DB, Senkov ON. A critical review of high entropy alloys and related concepts. *Acta Mater* 2017;122:448–511.
- [16] Li Z, Zhao S, Ritchie RO, Meyers MA. Mechanical properties of high-entropy alloys with emphasis on face-centered cubic alloys. *Prog Mater Sci* 2019;102:296–345.
- [17] Ma E, Wu X. Tailoring heterogeneities in high-entropy alloys to promote strength–ductility synergy. *Nat Commun* 2019;10(1):5623.
- [18] Lee H, Kim M, Sharma A, Ahn B. Oxidative and abrasive wear of multiphase $\text{AlSi}_{0.75}\text{TiMnFeC}_{x}$ ($X = 0, 0.25, 0.5$) high entropy alloy under non-lubricating reciprocating motion. *Powder Metall* 2023;66(5):623–34.
- [19] Zheng X, Gong M, Xiong T, Ge H, Yang L, Zhou Y, et al. Deformation induced FCC lamellae and their interaction in commercial pure Ti. *Scripta Mater* 2019;162:326–30.
- [20] Bai F, Yin L, Zhao W, Zhou H, Song M, Liu Y, et al. Deformational behavior of face-centered cubic (FCC) phase in high-pure titanium. *Mater Sci Eng, A* 2021;800.
- [21] Zhang Z, Mao MM, Wang J, Gludovatz B, Zhang Z, Mao SX, et al. Nanoscale origins of the damage tolerance of the high-entropy alloy CrMnFeCoNi. *Nat Commun* 2015;6(1):10143.
- [22] Gali A, George EP. Tensile properties of high- and medium-entropy alloys. *Intermetallics* 2013;39:74–8.
- [23] Oh MC, Sharma A, Lee H, Ahn B. Phase separation and mechanical behavior of AlCoCrFeNi-X ($X = \text{Cu}, \text{Mn}, \text{Ti}$) high entropy alloys processed via powder metallurgy. *Intermetallics* 2021;139:107369.
- [24] Shun T-T, Chang L-Y, Shiu M-H. Microstructures and mechanical properties of multiprincipal component CoCrFeNiTix alloys. *Mater Sci Eng, A* 2012;556:170–4.
- [25] Sun ZH, Zhang J, Xin GX, Xie L, Yang LC, Peng Q. Tensile mechanical properties of CoCrFeNiTiAl high entropy alloy via molecular dynamics simulations. *Intermetallics* 2022;142:107444.
- [26] Karimzadeh M, Malekan M, Mirzadeh H, Li L, Saini N. Effects of titanium addition on the microstructure and mechanical properties of quaternary CoCrFeNi high entropy alloy. *Mater Sci Eng, A* 2022;856:143971.
- [27] Salifu S, Olubambi PA. Effects of fabrication techniques on the mechanical properties of high entropy alloys: a review. *Int J Lightweight Mater Manuf* 2023. <https://doi.org/10.1016/j.ijlmm.2023.08.001>.
- [28] Liu H, Yang D, Jiang Q, Jiang Y, Yang W, Liu L, et al. Additive manufacturing of metallic glasses and high-entropy alloys: significance, unsettled issues, and future directions. *J Mater Sci Technol* 2023;140:79–120.
- [29] Guo S, Sui S, Wang M, Wang Q, Tang R, Guo A, et al. Simultaneously optimizing the strength and ductility of high-entropy alloys by magnetic field-assisted additive manufacturing. *J Alloys Compd* 2023;947:169688.
- [30] Chen C, Xie Y, Yin S, Li W, Luo X, Xie X, et al. Ductile and high strength Cu fabricated by solid-state cold spray additive manufacturing. *J Mater Sci Technol* 2023;134:234–43.
- [31] Li W, Yang K, Yin S, Yang X, Xu Y, Lupoi R. Solid-state additive manufacturing and repairing by cold spraying: a review. *J Mater Sci Technol* 2018;34(3):440–57.
- [32] Ahn J-E, Kim Y-K, Yoon S-H, Lee K-A. Tuning the microstructure and mechanical properties of cold sprayed equiautomic CoCrFeMnNi high-entropy alloy coating layer. *Met Mater Int* 2021;27(7):2406–15.
- [33] Rojas DF, Li H, Orhan OK, Shao C, Hogan JD, Ponga M. Mechanical and microstructural properties of a CoCrFe_{0.75}NiMo_{0.3}Nb_{0.125} high-entropy alloy additively manufactured via cold-spray. *J Alloys Compd* 2022;893:162309.
- [34] Feng S, Guan S, Story WA, Ren J, Zhang S, Te A, et al. Cold spray additive manufacturing of CoCrFeNiMn high-entropy alloy: process development, microstructure, and mechanical properties. *J Therm Spray Technol* 2022;31:1222–31.
- [35] Li Y-J, Luo X-T, Rashid H, Li C-J. A new approach to prepare fully dense Cu with high conductivities and anti-corrosion performance by cold spray. *J Alloys Compd* 2018;740:406–13.
- [36] Chu X, Che H, Yue S. Understanding the cold spray deposition characteristics of mixed metal powders. *MRS Adv* 2019;4:2989–95.
- [37] Story WA, Brewer LN. Heat treatment of gas-atomized powders for cold spray deposition. *Metall Mater Trans A* 2018;49:446–9.
- [38] Wei Y-K, Luo X-T, Ge Y, Chu X, Huang G-S, Li C-J. Deposition of fully dense Al-based coatings via in-situ micro-forging assisted cold spray for excellent corrosion protection of AZ31B magnesium alloy. *J Alloys Compd* 2019;806:1116–26.
- [39] Bray M, Cockburn A, O'Neill W. The laser-assisted cold spray process and deposit characterisation. *Surf Coat Technol* 2009;203(19):2851–7.
- [40] Sun W, Tan AW-Y, Wu K, Yin S, Yang X, Marinescu I, et al. Post-process treatments on supersonic cold sprayed coatings: a review. *Coatings* 2020;10(2):123.
- [41] Zhang J, Kong D. Effect of laser remelting on microstructure and immersion corrosion of cold-sprayed aluminum coating on S355 structural steel. *Opt Laser Technol* 2018;106:348–56.
- [42] Yang K, Li W, Xu Y, Yang X. Using friction stir processing to augment corrosion resistance of cold sprayed AA2024/Al₂O₃ composite coatings. *J Alloys Compd* 2019;774:1223–32.
- [43] Tariq N, Gyansah L, Qiu X, Du H, Wang J, Feng B, et al. Thermo-mechanical post-treatment: a strategic approach to improve microstructure and mechanical properties of cold spray additively manufactured composites. *Mater Des* 2018;156:287–99.
- [44] Petrovskiy P, Sova A, Doubenskaia M, Smurov I. Influence of hot isostatic pressing on structure and properties of titanium cold-spray deposits. *Int J Adv Manuf Technol* 2019;102:819–27.
- [45] Chu X, Meng F, Chi Z, Aydin H, Wei Y-K, Vo P, et al. Effects of powder characteristics and mixing powders on cold sprayability and corrosion properties of tantalum coatings. *Surf Coat Technol* 2021;426:127763.
- [46] Chu X, Che H, Teng C, Vo P, Yue S. Understanding particle-particle interactions from deposition efficiencies in cold spray of mixed Fe/316L powders with different particle size combinations. *J Therm Spray Technol* 2020;29:413–22.
- [47] Xu Y, Li W, Qu L, Yang X, Song B, Lupoi R, et al. Solid-state cold spraying of FeCoCrNiMn high-entropy alloy: an insight into microstructure evolution and oxidation behavior at 700–900 °C. *J Mater Sci Technol* 2021;68:172–83.
- [48] Wei Y-K, Li Y-J, Zhang Y, Luo X-T, Li C-J. Corrosion resistant nickel coating with strong adhesion on AZ31B magnesium alloy prepared by an in-situ shot-peening-assisted cold spray. *Corrosion Sci* 2018;138:105–15.
- [49] Luo X-T, Wei Y-K, Wang Y, Li C-J. Microstructure and mechanical property of Ti and Ti₆Al₄V prepared by an in-situ shot peening assisted cold spraying. *Mater Des* 2015;85:527–33.
- [50] Xie X, Yin S, Raelison R-n, Chen C, Verdy C, Li W, et al. Al matrix composites fabricated by solid-state cold spray deposition: a critical review. *J Mater Sci Technol* 2021;86:20–55.
- [51] Huang R, Sone M, Ma W, Fukunuma H. The effects of heat treatment on the mechanical properties of cold-sprayed coatings. *Surf Coat Technol* 2015;261:278–88.
- [52] Wu D, Li W, Liu K, Yang Y, Hao S. Optimization of cold spray additive manufactured AA2024/Al₂O₃ metal matrix composite with heat treatment. *J Mater Sci Technol* 2022;106:211–24.
- [53] Kini MK, Lee S, Savan A, Breitbach B, Addab Y, Lu W, et al. Nanocrystalline equiautomic CoCrFeNi alloy thin films: are they single phase fcc? *Surf Coat Technol* 2021;410:126945.
- [54] Stein F, Leineweber A. Laves phases: a review of their functional and structural applications and an improved fundamental understanding of stability and properties. *J Mater Sci* 2020;56(9):5321–427.
- [55] Laplanche G, Berglund S, Reinhart C, Kostka A, Fox F, George EP. Phase stability and kinetics of σ -phase precipitation in CrMnFeCoNi high-entropy alloys. *Acta Mater* 2018;161:338–51.
- [56] Liu G, Xiao M, Biroscas S. The nucleation and growth of η phase in nickel-based superalloy during long-term thermal exposure. *Acta Mater* 2020;185:493–506.
- [57] Ahn J-E, Kim Y-K, Yoon S-H, Lee K-A. Tuning the microstructure and mechanical properties of cold sprayed equiautomic CoCrFeMnNi high-entropy alloy coating layer. *Met Mater Int* 2020;27(7):2406–15.
- [58] Paul T, Joshi R, Walde C, Zhang C, Birt A, Pepi M, et al. Multi-scale elastic behavior of cold sprayed refractory metal from splat to bulk deposit by integrated experimental and modeling approach. *Mater Sci Eng, A* 2022;853:143751.
- [59] Li W, Kou H, Zhang X, Ma J, Li Y, Geng P, et al. Temperature-dependent elastic modulus model for metallic bulk materials. *Mech Mater* 2019;139:103194.
- [60] Yu B, Tam J, Li W, Cho HJ, Legoux JG, Poirier D, et al. Microstructural and bulk properties evolution of cold-sprayed copper coatings after low temperature annealing. *Materialia* 2019;7:100356.
- [61] Gussev MN, Leonard KJ. In situ SEM-EBSD analysis of plastic deformation mechanisms in neutron-irradiated austenitic steel. *J Nucl Mater* 2019;517:45–56.

- [62] Say Y, Dikici B, Kaseem M, Özkul İ, Güler Ö. Production of CoCrFeNi(Al/Ti) high-entropy alloys by mechanical alloying: optimization of milling time and comparison of corrosion susceptibilities. *J Mater Eng Perform* 2023. <https://doi.org/10.1007/s11665-023-08380-9>.
- [63] Liu H, Gao W, Liu J, Du X, Li X, Yang H. Microstructure and properties of CoCrFeNiTi high-entropy alloy coating fabricated by laser cladding. *J Mater Eng Perform* 2020;29:7170–8.
- [64] Yan X, Zhang X, Wang F, Stockdale T, Dzenis Y, Nastasi M, et al. Fabrication of ODS austenitic steels and CoCrFeNi high-entropy alloys by spark plasma sintering for nuclear energy applications. *JOM* 2019;71:2856–67.
- [65] Laplanche G, Gadaud P, Bärsch C, Demtröder K, Reinhart C, Schreuer J, et al. Elastic moduli and thermal expansion coefficients of medium-entropy subsystems of the CrMnFeCoNi high-entropy alloy. *J Alloys Compd* 2018;746:244–55.
- [66] Li J, Ouyang D, Wang Q, Teng Q, Cai C, Wei Q. Achieving superior tensile strength of CoCrFeNiTi_{0.3} high-entropy alloy via in-situ laser powder bed fusion of CoCrFeNi and Ti. *Mater Sci Eng, A* 2023;886:145649.
- [67] Li H, Zhang S, Liang J, Hu M, Yang Y. Effect of Ti on characterization and properties of CoCrFeNiTi_x high entropy alloy prepared via electro-deoxidization of the metal oxides and vacuum hot pressing sintering process. *Materials* 2023;16(4):1547.
- [68] Zhang H, Liu P, Hou J, Qiao J, Wu Y. Prediction of strength and ductility in partially recrystallized CoCrFeNiTi_{0.2} high-entropy alloy. *Entropy* 2019;21(4):389.